uOttawa

L'Université canadienne
Canada's university

FACULTÉ DES ÉTUDES SUPÉRIEURES ET POSTOCTORALES

uOttawa

L'Université canadienne
Canada's university

FACULTY OF GRADUATE AND POSDOCTORAL STUDIES

Michael Corrigan

AUTEUR DE LA THÈSE / AUTHOR OF THESIS

M.Sc. (Physics)

GRADE / DEGREE

Department of Physics

FACULTÉ, ÉCOLE, DÉPARTEMENT / FACULTY, SCHOOL, DEPARTMENT

Measurements of Absorption Line Frequency Shifts and Line Broadening Effects Using Frequency Stabilized 1.5 Micron Lasers

TITRE DE LA THÈSE / TITLE OF THESIS

Dr. A. Czajkowski

DIRECTEUR (DIRECTRICE) DE LA THÈSE / THESIS SUPERVISOR

CO-DIRECTEUR (CO-DIRECTRICE) DE LA THÈSE / THESIS CO-SUPERVISOR

EXAMINATEURS (EXAMINATRICES) DE LA THÈSE / THESIS EXAMINERS

Dr. X. Bao

Dr. S. Charbonneau

Dr. G. Oakham

Gary W. Slater

Le Doyen de la Faculté des études supérieures et postdoctorales / Dean of the Faculty of Graduate and Postdoctoral Studies

Measurements of Absorption Line Frequency Shifts and Line Broadening Effects Using Frequency Stabilized 1.5 Micron Lasers

Michael A. Corrigan

Thesis submitted to the Faculty of Graduate and Postdoctoral Studies in partial fulfillment of the requirements for the MSc degree in Physics

Faculty of Science
University of Ottawa

Your file Votre référence
ISBN: 978-0-494-34064-6
Our file Notre référence
ISBN: 978-0-494-34064-6

Table of Contents

List of Figures and Tables

Abstract

This work deals primarily with measurements of molecular line's frequency shifts induced by pressure, laser power and applied frequency modulation. The subjects of the study were infrared transitions in acetylene (C_2H_2) and ammonia (NH_3) molecules, which are important from the point of view of telecommunications and metrology researchers. In addition, the measurements of saturated line power broadening were carried out for selected lines of $^{12}C_2H_2$ and $^{13}C_2H_2$ as well as for the recently discovered saturated absorption line in $^{14}NH_3$. This study led to experimentally establishing the molecular dipole moments for a given transition even without proper ro-vibrational assignment.

Acknowledgments

I would like to express a great deal of thanks to my supervisor Andrzej Czajkowski. He has been truly devoted to this project in every aspect. I am very grateful for his patience, guidance, and expertise regarding everything from lab techniques to understanding physical concepts to writing assistance. I would also thank everyone in the Frequency and Time group, particularly Dr. John Bernard, Dr. Alan Madej, and Andrew Shiner for their support in the lab and during conferences.

I would also like to thank all the professors, secretaries, students, and all members of the physics department at the University of Ottawa for providing a friendly and receptive environment that I have had the privilege of participating in for the past 6 years during my undergrad and graduate studies.

Last, but not least, I will thank my family, friends, and loved ones for encouragement and inspiration.

1. Introduction

The field of laser frequency stabilization is almost as old as laser physics itself. The first Lamb-dip stabilized He-Ne lasers were developed in 1964. In 1968 quick advances in the field, such as the use of separate gain mechanisms and absorption tubes inside the laser cavity, led to reproducibility of 1 in 10^{-11} and stability in the 1 in 10^{-13} range for laser systems. In the following years, there was continuous effort in a number of leading laboratories towards development of a rich array of laser stabilization methods for every possible laser system [1]. For the next two decades, optical frequency standards groups were busy measuring the frequencies of various atomic and molecular transitions with reference to the Cesium (Cs) based definition of the second. To span a huge gap of frequency between the Cs-clock (9 192 631 770 Hz) and visible optical frequencies (well above 100 THz), frequency chains were developed. Simultaneously, frequency stabilized lasers were used in high precision measurements in atomic and molecular physics allowing for new, subtle effects to be experimentally investigated. The control of laser frequency resulted in some new and revolutionary developments in atomic physics, namely laser cooling and trapping, which ultimately led to a new class of atomic clocks operating in fountain configuration with long term stability of ~1 in 10^{-15}. The use of spectrally narrow and stable lasers to probe forbidden transitions in single trapped ions has introduced in site realization of optical clocks. "More accurate timepieces could lead to better global positioning systems, insights into fundamental physics and a redefinition of the second. It is perhaps not the ultimate race against time, but rather the race to keep ultimate time...In a handful of labs around the world; physicists are developing a new

generation of clocks so accurate that they should lose just one second in 100 billion years. By taking the pulse of laser light synchronized to the beating of atoms or ions, the researchers are confident that they can create clocks up to 1000 times more accurate than today's best timepieces," [2].

Among the prospects provided by the state-of-the-art laser stabilization techniques are accurate measurements of fundamental constants, insight into the time evolution of such constants, observation of gravitational waves and insights into the structure of the universe. Advances in "absolute phase" control of femtosecond pulses and recent generation of attosecond pulses open a window to investigation of quantum mechanical processes on the time-scale of the electronic density cloud reorganization during electronic excitation. This may lead to a new look at the half-century old interpretation of quantum mechanics. Leading national standards laboratories all over the world continue to push towards the development of new clocks, but for the sake of scientific progress, one should hope that the marvelously accurate methods of laser stabilization will continue to be used outside the field of timekeeping and absolute frequency measurements. It is a thrilling prospect as they have potential to push the frontier of experimental science into territories which only yesterday were occupied by science fiction writers.

Amongst the selection of frequency references mentioned earlier, the state-of-the-art is set by single ion standards (including: strontium, mercury, and ytterbium ions [3,4]), cesium and rubidium fountains [5,6], and most recently, strontium optical lattice standards [7]. These standards offer fractional frequency uncertainty of 10^{-15} to 10^{-16} with promise of further improvements in the near future. Specific molecular transitions

continue to play an important role as frequency references across the optical spectrum. For example, iodine stabilized lasers are employed as a length standard [8] and narrow transitions of the OsO_4 molecule serve as important infrared region frequency references [9]. Recently, molecular transitions in acetylene, rubidium, and hydrogen cyanide have been accepted as recommended standards for the near infrared telecom region [10].

The 1.5 μm spectral region is a prominent wavelength extensively used in telecommunication, imaging, satellite navigation systems, and in many optical devices. Notably, with the recent advancement of wave division multiplexing (a method employing closely spaced frequencies to serve as communication channels within fibre optic cables), high precision frequency references and stabilization methods are being sought. One of these has attracted particular attention has been attracted by the saturated absorption transition in acetylene (C_2H_2). Due to the very large number of absorption lines within the P and R branches (rotational modes) of the combination vibrational band $\nu_1 + \nu_3$ (**Figure 1**), and the fact they have linewidths below 1 MHz, these lines have offered a promise of a grid of closely spaced frequency markers with fractional uncertainty of 10^{-13} [11]. The region of these resonances also match the International Telecommunication Union's C band (1530-1560 nm), which has made it appealing for the telecommunication industry [12,13]. Acetylene has also received attention from several international metrology bodies, most notably from the Comite International des Poids et Mesures (CIPM), which has accepted the $\nu_1 + \nu_3$ P(16) transition in $^{13}C_2H_2$ as an official reference for the 1.5 μm region (*2001*) [14]. Other recommendations for this transition came from the Consultative Committee for Length (CCL) [14], as a realization for a length standard, and the International Committee for Weights and Measures [14,15].

As a result, acetylene is widely employed as one of the recommended optical frequency radiations. The work on acetylene is carried out by all major optical frequency groups including: the National Research Council (NRC, Canada), the National Institute of Standards and Technology (NIST, USA), the National Physics Laboratory (NPL, UK), the National Institute of Advanced Industrial Science and Technology (AIST, Japan), and the Physikalisch-Technische Bundesanstalt (PTB, Germany).

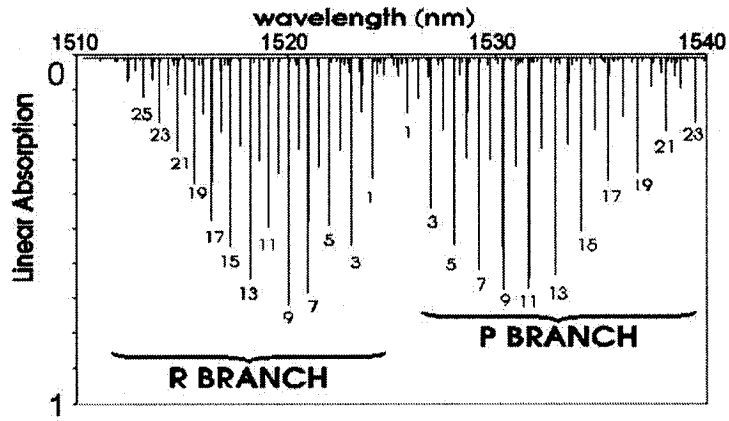

Figure 1: Absorption Lines of $^{12}C_2H_2$. The Doppler-broadened absorption spectrum of $^{12}C_2H_2$ was measured by recording light transmitted through a 45 cm long absorption cell at a pressure of 1 Torr. $^{13}C_2H_2$ has a similar spectrum but spans 1520-1550 nm. [11]

The NRC optical frequency standard group has actively participated in these developments since 2001 when two versatile and robust laser stabilization systems, utilizing cavity enhanced acetylene spectroscopy, were produced [11,16]. The cavity enhanced acetylene absorption has provided necessary power to allow for saturation of various overtone and combination bands in the near infrared region and led to frequency stabilization on these transitions. Both laser systems have been characterized and the measurements of frequency of over 100 acetylene lines were obtained using optical frequency combs [16].

The purpose of this research is to study various transition lines of acetylene molecules ($^{13}C_2H_2$ and $^{12}C_2H_2$) at high precision within the infrared region by saturated absorption laser spectroscopy and frequency-locking techniques. The primary goal is to investigate the effects of variations in the operating parameters on the laser frequency, while locked to a saturated absorption line of acetylene. These parameters included laser power, acetylene pressure, and modulation amplitude of the frequency. While pursuing these research goals, the stability and performance of the laser system were also carefully investigated.

In addition to the studies on acetylene transitions, high precision measurements of several ammonia (NH_3) transitions in the near- infrared region have been obtained for the first time. There are about 1700 weak absorption lines in the 1450-1560 nm region (**Figure 2**) known for ammonia. This alone makes the molecule an attractive candidate as a possible frequency standard for telecommunication usage, outside of the region spanned by the acetylene spectrum. To our knowledge, this was the first time that any of these transitions have been saturated and their saturated absorption features studied.

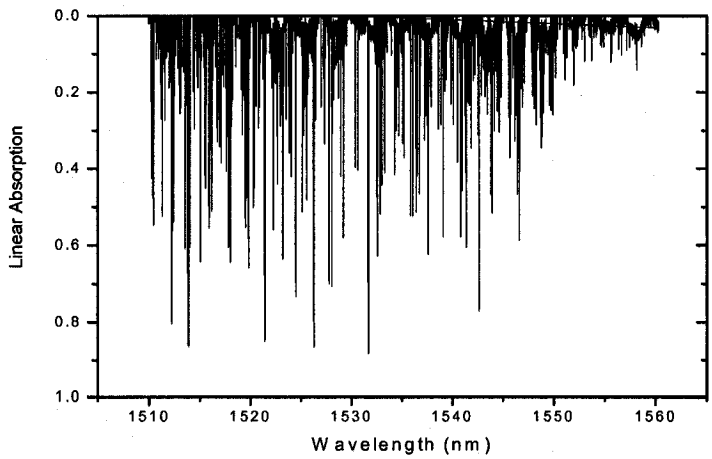

Figure 2: Normalized Doppler-Broadened Absorption Spectrum of NH_3. The profile was measured by recording the transmission intensity from a 1 m linear absorption cell filled with 10 Torr of NH_3 with laser output set at 13.1 mW.

2. Theory

2.1. A Brief Introduction to Structure and Energy of Polyatomic Molecules

2.1.1 The Born-Oppenheimer Approximation

Quantized internal energy levels of simple molecule and atomic systems have been successfully described from solutions to the Schrödinger equation, $H\Psi = E\Psi$; where the Hamiltonian operator, H, describes the total kinetic and potential energy of the system; Ψ is the wavefunction of the system, and E is the energy eigenvalue of the system.

A polyatomic molecule is a complex multi-body system. In such a system, it is often difficult to account for all the interactions involved and quite naturally it is impossible to analytically solve the Schrödinger equation. An example Hamiltonian for such a molecule is:

(Eqn. 1)

$$H = \underbrace{-\frac{\hbar^2}{2m_e}\sum_i \nabla_i^2}_{\substack{\text{(electron}\\ \text{kinetic}\\ \text{energy)}}} \underbrace{-\sum_A \frac{\hbar^2}{2M_A}\nabla_A^2}_{\substack{\text{(nuclear}\\ \text{kinetic}\\ \text{energy)}}} \underbrace{-\sum_{A,i} \frac{Z_A e^2}{r_{Ai}}}_{\substack{\text{(electron-}\\ \text{nuclear}\\ \text{attraction)}}} + \underbrace{\sum_{A>B} \frac{Z_A Z_B e^2}{R_{AB}}}_{\substack{\text{(nuclear-}\\ \text{nuclear}\\ \text{repulsions)}}} + \underbrace{\sum_{i>j} \frac{e^2}{r_{ij}}}_{\substack{\text{(electron-}\\ \text{electron}\\ \text{repulsions)}}} \quad [17];$$

where the summations are summed over each nucleus (A,B) and each electron (i,j), ħ is Planck's constant, m_e is the mass of the electron, M is the mass of the nucleus, Z is the atomic number, e is the charge of the electron, r is the radial co-ordinate of the electron, and R is the radial co-ordinate of the nucleus, each with respect to the centre of mass.

To gain insight into such a system, and to determine values of energy levels of the molecule, the Born-Oppenheimer approximation is used. The Born-Oppenheimer approximation relies on the fact that electrons are less massive and therefore have much

larger average velocities compared to the nuclei. The nuclei are essentially stationary during electronic transitions and provide a constant Coulomb field for the electrons to interact with. Mathematically this approximation implies separating the variables of the nuclear and electronic coordinates so that the total molecular wavefunction, Ψ, may be expressed as:

(Eqn. 2) $\Psi(r,R) = \psi_e(r;R)\chi_n(R)$ [17];

where ψ_e describes the electron wavefunction, χ_n describes the nuclear wavefunction. The nuclear wavefunction may be further separated into vibrational, rotational, and nuclear spin terms so that the total wavefunction is expressed as:

(Eqn. 3) $\Psi = \psi_{electron}\psi_{rotation}\psi_{vibration}\psi_{\substack{nuclear \\ spin}}$ [17].

Utilizing this wavefunction in the Schrödinger equation leads to an expansion of molecular energy states:

(Eqn. 4)

$$H\Psi = E\Psi$$

$$H\left(\psi_{electron}\psi_{rotation}\psi_{vibration}\psi_{\substack{nuclear \\ spin}}\right) = \left(E_{electron} + E_{rotation} + E_{vibration} + E_{\substack{nuclear \\ spin}}\right)\left(\psi_{electron}\psi_{rotation}\psi_{vibration}\psi_{\substack{nuclear \\ spin}}\right)$$

[17].

The constitution of a given molecular state (neglecting nuclear spin) involves contributions from electronic (T_e), vibrational (G_v), and rotational terms ($F_v(J)$):

(Eqn. 5) $E = T_e + G_v + F_v(J)$ [17].

The rotational energy of this state is modeled by the quantum non-rigid rotor (**Figure 3**) and is described by its rotational quantum number J. The vibrational energy is modeled by the anharmonic quantum oscillator and is described by the vibrational quantum number v.

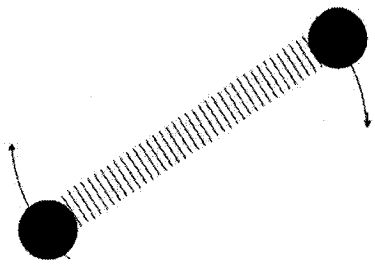

Figure 3: The Non-Rigid Rotor. A non-rigid rotor with two particles on ends that may oscillate between each other. A vibration-rotation interaction occurs due to stretching of the bond length by centrifugal force in the rotating rotor.

The model of a polyatomic molecule is much more complicated than that of a diatomic molecule due to the increasing number of degrees of freedom with each additional atom. The commonly used expression for a molecular state is:

(Eqn. 6)

$$E = T_e + \left[\sum_i \omega_i\left(\nu_i + \frac{d_i}{2}\right) + \sum_i \sum_{k>i} \omega\chi_{ik}\left(\nu_i + \frac{d_i}{2}\right)\left(\nu_k + \frac{d_k}{2}\right) + \ldots\right] + \frac{1}{2}(B_\nu + C_\nu)J(J+1) + \left[A_\nu - \frac{1}{2}(B_\nu + C_\nu)\right]\omega(J,K) \quad [17].$$

This expression includes the vibration-rotation interaction in the ν_i dependent rotational constants A, B, and C. ω is the frequency of anharmonic oscillator and $\omega(J,K)$ is either symmetric or asymmetric rotor energy depending on the model being used. The degeneracy of each vibration is represented by d_i and $\omega\chi$ is the anharmonicity factor.

2.1.2. Molecular Transitions

A molecular transition may involve simultaneous changes in electronic, vibrational, and rotational states. **Figure 4** illustrates a given electronic state, of Leonard-Jones type

potential, with a manifold of vibrational-rotational states. Within an electronic transition of states from A to B (**Figure 5**), there are many vibrational and rotation states that may also change (i to j in our example). Due to the simultaneous changes of states, a spectrum of closely spaced lines emerges, rather than an individual line that would be associated with an electronic transition alone.

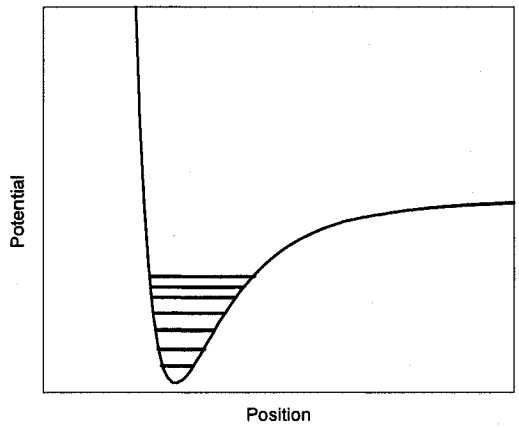

Figure 4: An Electronic State within a Diatomic Molecule. This figure shows a single electronic state of a diatomic molecule with Leonard-Jones potential. Within the electronic state, there exist many nuclear rotational-vibrational states [17].

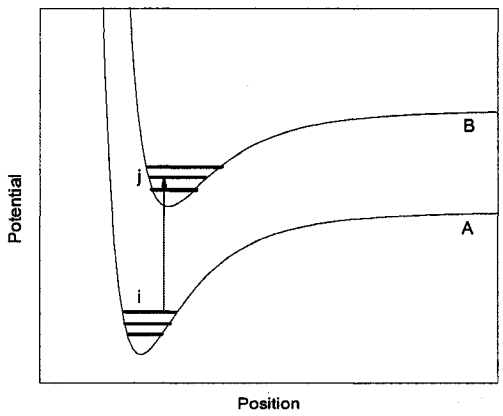

Figure 5: Transition between Electronic States within a Diatomic Molecule. This figure shows a transition between electronic state A and B and simultaneous transitions of the rotational-vibrational state (i to j) of a diatomic molecule [17].

2.1.3. Intensity of Absorption Lines

The intensity of absorption of radiation for a molecular transition is determined by the change in electric-dipole between initial, i, and final, f, states. The intensity may be calculated from the square of the matrix element:

(Eqn. 7) $\mu_{if} = \int \Psi^{*'} \mu \Psi'' dV$ [17];

where μ is the total dipole moment with electronic, μ_e, and nuclear terms, μ_n:

(Eqn. 8) $\mu = \mu_e + \mu_n = -\sum_i e r_i + \sum_\alpha e Z_\alpha R_\alpha$ [17].

Calculations of the intensity of a transition are greatly simplified by employing the Born-Oppenheimer approximation to separate wavefunctions into electronic and vibrational, components:

(Eqn. 9) $\mu_{if} = \int (\psi_{electron}\psi_{vibration})^{*'} \mu (\psi_{electron}\psi_{vibration})'' dr dR$ [17];

where the integral is over the nuclear and electronic coordinates.

This greatly simplifies the evaluation of the dipole moment:

(Eqn. 10) $\mu_{if} = \int \psi^{*'}_{electron}\psi^{*'}_{vibration}(\mu_e + \mu_n)\psi^{*''}_{electron}\psi^{*''}_{vibration} dr dR$ [17],

$$\mu_{if} = \int \left(\int \psi^{*'}_{electron} \mu_e \psi^{*''}_{electron} dr \right) \psi^{*'}_{vibration}\psi^{*''}_{vibration} dR + \int \psi^{*'}_{electron}\psi^{*''}_{electron} dr \int \psi^{*'}_{vibration} \mu_n \psi^{*''}_{vibration} dR$$

[17].

The overlap integral of the two electronic wavefunctions, in the second term, will vanish because these two functions are orthogonal.

If we define the electronic transition moment:

(Eqn. 11) $M_e(R) = \int \psi^{*'}_{electron} \mu_e \psi^{*''}_{electron} dr$ [17].

The overall transition moment becomes:

(Eqn. 12) $\mu_{if} = \int M_e(R)\psi^{*'}_{vibration}\psi^{*''}_{vibration}dR$ [17].

Within the Born-Oppenheimer approximation, the R-dependence of $M_e(R)$ is small. As a result, this term may be removed outside of the integral:

(Eqn. 13) $\mu_{if} = M_e\int\psi^{*'}_{vibration}\psi^{*''}_{vibration}dR$ [17].

The relative intensities of transitions between the vibrational states $\psi'_{vibration}$ and $\psi''_{vibration}$ (or v'and v'') are described by the Franck-Condon factor, $q_{v'v''}$, which is the square of the overlap of vibrational wavefunctions:

(Eqn. 14) $q_{v'v''} = \left|\int\psi^{*}_{vib'}\psi_{vib''}dR\right|^2 = \left|\langle v'\|v''\rangle\right|^2$ [17].

There are no selection rules for pairs of vibronic states according to which transitions will be coupled by electromagnetic radiation. However, rotational transitions do have selections rules for transitions coupling to electromagnetic radiation. The conditions for rotational transitions to accompany radiation are that the rotational angular momentum of the system, J, must follow: $\Delta J = -1, 0,$ or 1. These conditions shape the rotational-vibrational spectrum (simultaneous rotational and vibrational transitions) to consist of the P branch ($\Delta J = -1$), the Q branch ($\Delta J = 0$) and the R branch ($\Delta J = 1$) **(Figure 6)**.

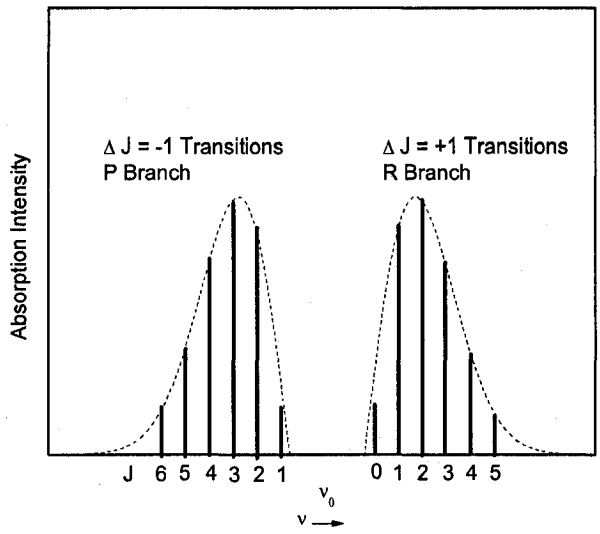

Figure 6: Spectrum of Rotational-Vibrational Transitions of a Simple Diatomic Molecule. This figure illustrates the P and R branches in which rotational-vibrational transitions are coupled with radiation. Absorption intensities in this plot are attributed by Boltzmann statistics of molecules in a rigid rotor system [18].

The spectra of simple polyatomic molecules, such as ones that contain few low Z atoms (i.e Hydrogen) often have recognizable P, Q, and R branches. As the molecular chain increases with number of atoms the spectrum becomes more complex and transitions begin to overlap causing merging into broad semi-continuum for large molecules.

Aside from the quantum mechanical effects, the strength of absorption (I) is also affected by the number of molecules in the initial state (N). For a gas in thermal equilibrium at temperature T, N is determined from the Boltzmann distribution:

(Eqn. 15) $$I \propto N_{\substack{lower \\ State}}$$ [17]

(Eqn. 16) $$I \propto g_i \exp\left(\frac{-E_i}{kT}\right)$$ [17];

where g_i is the degeneracy of the state and k is Boltzmann's constant.

In the case of rotational levels, modeled by the rigid rotor system, the absorption strength is:

(Eqn. 17) $$I = (2J+1)\exp\left(\frac{-BJ(J+1)}{kT}\right)$$ [17];

where B is a rotational constant of the system.

Another factor affecting the intensity of the absorption spectrum is the nuclear spin of the molecules. Nuclear spin must be included in our description of the molecular state because it has important consequences on the symmetry of the total wavefunction of the molecule.

Nuclei are composed of protons and neutrons which add up to the overall spin of the ensemble. In general, odd-mass-number nuclei are fermions, and even-mass-number nuclei are bosons [17]. The atomic nuclei either follow Fermi-Dirac statistics if they are fermions or Bose-Einstein statistics if they are bosons.

In the Born-Oppenheimer approximation, the molecular wavefunction is the product of electronic, rotational, vibrational, and nuclear spin (**Eqn. 3**). It is required by the Pauli principle that the total wavefunction under the operation of particle exchange is symmetric if the nuclei are bosons, and antisymmetric if the nuclei are fermions. The acetylene molecule ($^{12}C_2H_2$), for example, must have a total wavefunction that is symmetric under the C-H complex exchange [19]. The ground electronic and vibrational wavefunctions are symmetric with respect to this operation, but the rotational wavefunction is alternating between symmetric for even J states, and antisymmetric for odd J states. Accordingly, the nuclear spin wavefunction must be antisymmetric for even J states, and symmetric for odd J states to maintain overall symmetry of the total wavefunction. The nuclear spin wavefunction, ψ, may take on the following forms:

(Eqn. 18) (a) $\psi_{\substack{nuclear \\ spin}} = |1\uparrow\rangle|2\uparrow\rangle$

(b) $\psi_{\substack{nuclear \\ spin}} = |1\downarrow\rangle|2\downarrow\rangle$

(c) $\psi_{\substack{nuclear \\ spin}} = \frac{1}{\sqrt{2}}|1\uparrow\rangle|2\downarrow\rangle + \frac{1}{\sqrt{2}}|1\downarrow\rangle|2\uparrow\rangle$ [19,20];

(d) $\psi_{\substack{nuclear \\ spin}} = \frac{1}{\sqrt{2}}|1\uparrow\rangle|2\downarrow\rangle - \frac{1}{\sqrt{2}}|1\downarrow\rangle|2\uparrow\rangle$

where 1 and 2 refer to the two hydrogen atoms within the molecule, $|\uparrow\rangle$ represents the spin-up wavefunction of hydrogen and $|\downarrow\rangle$ represents the spin-down wavefunction of hydrogen (the ^{12}C atoms can be neglected because they have zero spin [19,20]).

The nuclear spin wavefunctions (a), (b), and (c) are symmetric under particle exchange and the wavefunction (d) is antisymmetric under exchange. As a result, the statistical weight of odd J rotational levels is three times that of even J levels. Thus the overall strength of absorption, for rotational and nuclear spin structure, may be described by:

(Eqn. 19) $$I = g_I(2J+1)\exp\left(\frac{-BJ(J+1)}{kT}\right)$$ [19];

where g_I is the degeneracy of nuclear spin states.

In the case of $^{12}C_2H_2$, $g_I = 1$ (for even J) or 3 (for odd J). The consequence of the nuclear spin degeneracy causes the absorption lines to alternate in intensity.

2.2. The Vibrational Modes of Acetylene

Acetylene is a symmetric linear molecule and has seven fundamental vibrational modes (**Table 1**). The motion of atoms within molecules are typically described by symmetry of

the structure. Vibrational modes that are symmetric are referred to as *gerade*, the German word for even. These modes include the ν_1, ν_2, and ν_4 vibrations and are identified by a "g" within the symmetry species column (**Table 1**). Vibrational modes that are antisymmetric, such as the ν_3 and ν_5 vibrational modes, are referred to as *ungerade* and are labeled with a "u". These modes are also labeled as Σ for those vibrating along the molecular axis (z-axis), or Π for those that bend normal to the molecular axis (x and y axis). The Π vibrations are degenerate because they may bend either on the x or y axis [19].

Table 1: Fundamental Vibrations of Acetylene [19,20].

Mode	Description	Symmetry	Normal Mode	Energy (cm^{-1})
ν_1	Symmetric C-H stretch	Σ_g^+	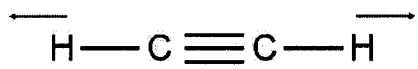	3374
ν_2	Symmetric C-C stretch	Σ_g^+	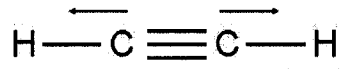	1974
ν_3	Asymmetric C-H stretch	Σ_u^+	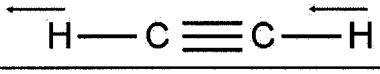	3287
ν_4	Symmetric bend	Π_g	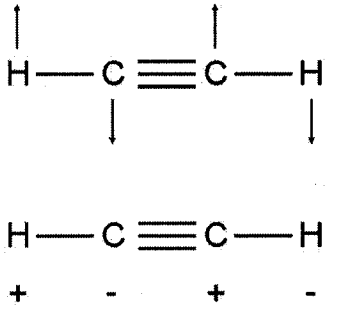	612
ν_5	Asymmetric bend	Π_u	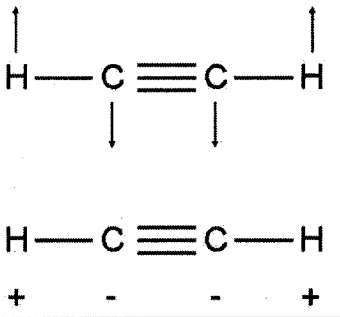	729

2.3. Ammonia (NH_3)

Ammonia is widely used within common household items such as refrigerators, fertilizers, and cleaning products. Some industrial applications of this chemical include its use in noncatalytic reduction systems, (i.e. Thermal $DeNO_x$ [21]), and in microchip manufacturing [22].

The increasing number of studies on absorption lines in ammonia within the near infrared region (1.3-2.0 μm) can be attributed to the need for monitoring levels of ammonia gas in many practices. Detection of this gas is important because of its toxicity and extensive use. Methods of detection are commonly employed in environmental monitoring [21] and in planetary research [23,24,25]. Such fields take advantage of characteristic absorption lines, within the near infrared region, to detect the presence of this molecule. Research on the near infrared spectrum of ammonia, and specific absorption lines, assists the design of detectors and allows gas tracing at levels of ppm and ppb [21,26,27].

The most extensive study of ammonia in the near infrared region was conducted in 1993 by L. Lundsberg-Nilesen, F. Heglund, and F.M. Nicolaisen [28]. This group obtained a spectrum of NH_3 over the 1450-1560 nm region, using a Fourier transform spectrometer, and observed a total of 1710 lines. Out of that number only 381 rotational-vibrational transitions have been assigned to the vibrational bands. This work serves as one of the most important references for ongoing investigations of NH_3 in the near infrared region.

Due to the complexity and richness of this spectrum there exists an inherent difficulty in resolving certain absorption lines that are over-lapping with neighbouring lines. As a result, a large number of lines remain without proper v and J assignment in the near infrared region. As of lately, the accuracy of some of the initial assignments reported in 1993 [28] has been questioned [21]. This emphasizes the need for further studies.

2.4. Saturation Spectroscopy

The introduction of the laser led to higher resolution techniques in spectroscopy and better understandings of molecular and atomic processes. One example of such a development that is utilized in our work is saturation spectroscopy. This technique allows selective saturation of transitions of molecules within a specific velocity class by optical pumping with a monochromatic tunable laser.

To describe this technique, consider a sample of a molecular gas residing in a cell at thermal equilibrium of temperature T. The ground state population of the molecules, n_1, has a Maxwellian distribution over the velocity component v_z:

(Eqn. 20) $$n_1(v_z) = \frac{N_1}{v_p\sqrt{\pi}} \exp\left[-\left(\frac{v_z}{v_p}\right)^2\right]$$ [29];

where N_1 is the total number of molecules in energy level E_1, and v_p is the most probable velocity ($v_p = (2kT/m)^{1/2}$); and m is the mass of the molecule.

The frequency dependent absorption coefficient, $\alpha_0(\omega)$, of this gas is:

(Eqn. 21) $$\alpha_0(\omega) = \alpha_0(\omega_0)\exp\left[-\left(\frac{\omega-\omega_0}{\delta\omega_D}\right)^2\right]$$ [29] ;

where $\alpha_0(\omega_0)$ is the maximum strength of absorption, ω_0 is the resonance frequency of the absorbing molecule's transition, and $\delta\omega_D$ is the Doppler broadened width ($\delta\omega_D = 2\sqrt{\ln(2)}\frac{\omega_0 v_p}{c}$; with v_p being the most probable velocity and c the speed of light).

Providing an optical pump through this cell, by a narrow tunable laser set at a frequency of ω and wavevector K (parallel to the z component) (**Figure 7**), excites molecules into a higher energy level E_k (E_k-$E_i = \hbar\omega_0$) and depletes the ground population of molecules with velocity components:

(Eqn. 22) $$v_z \pm dv_z = \frac{(\omega_0 - \omega \pm \delta\omega)}{K}$$ [29];

where ω_0 is the resonance frequency of the absorbing molecular transition and $\delta\omega$ is the linewidth of the molecule. In the case of slow molecules, the linewidth is due mainly to transit time broadening and pressure broadening.

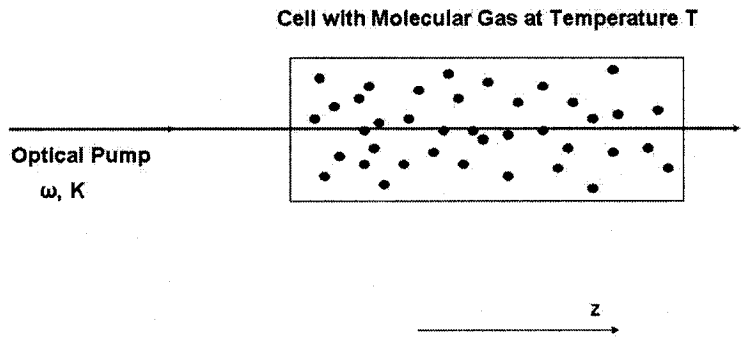

Figure 7: Optical Pumping of a Molecular Gas. An optical pump is sent through the cell to excite molecules with velocity component $v_z = (\omega_0 - \omega)/K$ [29].

In the case of an optical pump with narrow frequency tuned to ω_0, only molecules with velocity component $v_z = 0$ will be excited. The population distribution of the

ground state, in this situation, then has a depleted region at $v_z = 0$. The depleted region is known as the saturated absorption dip. To detect this feature, a second beam, called the probe beam, can be sent through the sample to probe the frequency dependence of the absorption of this gas. The absorption coefficient of the molecular gas in the presence of the standing wave field from the optical pump and the optical probe is:

(Eqn. 23) $$\alpha_s(\omega) = \alpha_0(\omega)\left[1 - \frac{S_0}{2}\left(1 + \frac{(\gamma_s/2)^2}{(\omega-\omega_0)^2 + (\gamma_s/2)^2}\right)\right]$$ [29];

where $\alpha_0(\omega)$ is the unsaturated absorption coefficient (as defined above), γ_s is the linewidth of the saturated absorption dip (due to pressure, saturation power, transit time and natural broadening), and S_0 is the saturation parameter (which is dependent on the power of the optical pump and the dipole moment of the given transition).

A plot of a sample absorption dip is shown in **Figure 8**.

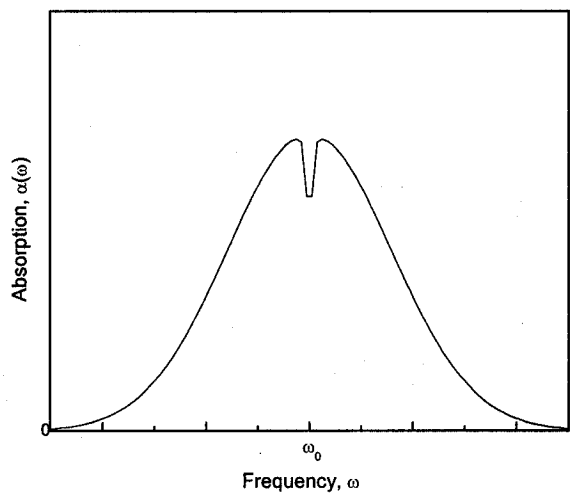

Figure 8: Absorption Profile about the Saturated Dip. Due to the excitation of $v_z = 0$ molecules from the optical pump there is reduced absorption strength at the frequency ω_0 [29].

The absorption coefficient features the saturated dip at frequency, ω_0, which results from a depleted number of molecules with velocity component $v_z = 0$ in the ground state. This feature is useful because the Doppler broadened line maximum uniquely specifies the line frequency (ω_0).

2.5. Line Broadening Mechanisms and Line Shifts

Absorption lines in molecular and atomic systems are never infinitely narrow. Even in saturation spectroscopy there exist several mechanisms which lead to broadening of the absorption line. The quantification of line profiles is typically done by means of describing the full width at half maximum (FWHM) of the absorption peak, also referred to as the linewidth or half-width. The main factors that contribute to broadening of the linewidth for a given absorption line, and/or saturation dip, include: natural broadening, Doppler broadening, pressure broadening, transit-time broadening, and power broadening. The nature of these mechanisms is described below.

2.5.1. Natural Broadening

During the process of radiation absorption by an atom or molecule, the atom/molecule undergoes a transition between lowered and excited state. Due to the finite time of excitation, there exists uncertainty in the energy value associated with each state (except the ground state) according to the Heisenberg uncertainty principle:

(Eqn. 24) $\Delta E \Delta t \approx \hbar$ [29].

For a mean lifetime (τ_i) of a molecule in the excited state with energy E_i, its energy can be resolved with an uncertainty of:

(Eqn. 25) $$\Delta E_i \approx \frac{\hbar}{\tau_i}$$ [29].

The frequency of the absorbed radiation within such a transition, E_i to E_k, is:

(Eqn. 26) $$\omega_{ik} = \frac{(E_i - E_k)}{\hbar}$$ [29].

The associated uncertainty with this frequency is:

(Eqn. 27) $$\delta\omega = \frac{\Delta E_i}{\hbar} = \frac{1}{\tau_i}$$ [29].

If the lower state of the transition, k, is not the ground state it will also have a mean lifetime, τ_k, in this state and an uncertainty of energy, ΔE_k, associated with it (similar to that of ΔE_i). Thus, the total uncertainty of energy, ΔE, of the absorption frequency is:

(Eqn. 28) $\Delta E = \Delta E_i + \Delta E_k$ [29].

Accordingly, the total uncertainty of absorbed radiation frequency, $\delta\omega_N$, is:

(Eqn. 29) $$\delta\omega_N = \left(\frac{1}{\tau_i} + \frac{1}{\tau_k}\right)$$ [29].

For this mechanism, the spectral profile of absorption is described by the Lorentzian function with linewidth $\delta\omega_N$:

(Eqn. 30) $$I(\omega) = \frac{1}{2\pi} \frac{\delta\omega_N}{(\omega_{ik} - \omega)^2 + \left(\frac{\delta\omega_N}{2}\right)^2}$$ [29].

The natural linewidth determines the limit of resolution in spectroscopy.

2.5.2. Doppler Broadening

One of the most significant mechanisms that contribute to broadening of an absorption line's profile is Doppler broadening. This relativistic effect is attributed to the thermal motion of the absorbing atoms/molecules.

This effect may be understood by considering a source of radiation traveling along the z-direction and incident on an absorbing molecular gas. The electric field of the radiation is described by the plane wave $E = E_0 \exp(i\omega t - k_z z)$ (where ω is its frequency, $k_z = \omega/c$ is its wavevector, c is the speed of light, and t and r are the time and position co-ordinates respectively). If the absorbing molecules have a velocity $v = (v_x, v_y, v_z)$ within the rest frame of an observer, the frequency of the radiation ω, in the frame of the molecule, is Doppler-shifted to a different frequency, ω':

(Eqn. 31) $$\omega' = \omega - k_z v_z = \omega\left(1 - \frac{v_z}{c}\right)$$ [29].

For the molecule to absorb the radiation, the condition $\omega' = \omega_0$ must be met (where ω_0 is the molecule's absorption frequency of a certain transition). Therefore, molecules will absorb radiation with frequency:

(Eqn. 32) $$\omega \cong \omega_0\left(1 + \frac{v_z}{c}\right)$$ [29];

the above equation uses the approximation: $\left(\frac{v}{c}\right)^2 \approx 0$.

If the molecular gas is at thermal equilibrium at a temperature T, it will have a Maxwellian velocity distribution:

(Eqn. 33) $$n(v_z) = \frac{N}{v_p\sqrt{\pi}} \exp\left[-\left(\frac{v_z}{v_p}\right)^2\right]$$ [29];

where N is the total number of molecules and $v_p = (2kT/m)^{1/2}$ is the most probable velocity; with k being Boltzmann's constant and m the molecule's mass.

The velocity distribution creates a dispersal of molecules with different absorbing frequencies, for a specific excitation, and is reflected in the absorption coefficient. Combing **Eqn. 32** and **Eqn. 33** to give the distribution as a function of absorption frequency, ω, of the molecules yields:

(Eqn. 34) $$n_i(\omega) = \frac{N_i c}{\omega_0 v_p \sqrt{\pi}} \exp\left(-\frac{c(\omega-\omega_0)^2}{\omega_0 v_p}\right)$$ [29].

Since the absorption of radiation is proportional to the density of molecules in a state, n(ω), the line profile solely due to Doppler broadening is Gaussian:

(Eqn. 35) $$I(\omega) = I_0 \exp\left(-\frac{c(\omega-\omega_0)^2}{\omega_0 v_p}\right)$$ [29].

The FWHM, $\delta\omega_D$, of this profile is:

(Eqn. 36) $$\delta\omega_D = 2\sqrt{\ln 2}\,\frac{\omega_0 v_p}{c} = \frac{\omega_0}{c}\sqrt{\frac{8kT\ln 2}{m}}$$ [29].

2.5.3. Transit Time Broadening

Transit time broadening, or time-of-flight broadening, originates from the finite interaction time of a molecule with an electromagnetic field.

To quantify the contribution of broadening from this effect one may describe an analogous system of an undamped oscillator. Consider that this oscillator is initially stationary and then for a finite time, T, it oscillates according to: $x(t) = x_0 \cos\omega_0 t$. After the time duration, T, the oscillator stops oscillating. The frequency spectrum, $A(\omega)$, of this oscillator is the Fourier transform of x(t) over the interval T:

(Eqn. 37) $$A(\omega) = \frac{1}{\sqrt{2\pi}} \int_0^T x_0 \cos(\omega_0 t) \exp(-i\omega t) dt$$ [29].

The spectral intensity profile, $I(\omega) = A^* A$, is:

(Eqn. 38) $$I(\omega) = C \frac{\sin^2[(\omega - \omega_0)T/2]}{(\omega - \omega_0)^2}$$ [29];

where C is a constant. The FWHM of this function is $\delta\omega = 5.6/T$ [29].

This example is analogous to an atom, or molecule, that encounters a beam of radiation for a finite time:

(Eqn. 39) $$T = \frac{2w_0}{\bar{v}}$$ [29];

where w_0 is the radius of the beam profile, and $\bar{v}$ is the mean velocity of the molecules traveling across the radiation field. The average velocity ($\bar{v}$) is given by:

(Eqn. 40) $$\bar{v} = \sqrt{\frac{8R'T}{\pi M'}}$$ [29];

where R' is the universal gas constant, T is the temperature of the gas at thermal equilibrium, and M' is the molar mass.

If this interaction time is small compared to the relaxation time of the molecule, then the atom acts like an undamped oscillator which oscillates proportionally to the electric field of the radiation, $E = E_0(r)\cos\omega t$. However, to more accurately describe the spatial

distribution of the laser intensity, the amplitude of the electric field is not constant (as it was in the analogous case: $x(t) = x_0 \cos\omega_0 t$) but varies according to a Gaussian beam profile:

(Eqn. 41) $$E = E_0 \exp\left(\frac{-r^2}{w_0^2}\right)\cos\omega t$$ [29].

Substituting this function **(Eqn. 41)** into **Eqn. 37** yields a Gaussian profile:

(Eqn. 42) $$I(\omega) = B\exp\left[-\frac{(\omega-\omega_0)^2 w_0^2}{2\bar{v}^2}\right]$$ [29];

where B is a constant.

The linewidth for this profile is:

(Eqn. 43) $$\delta\omega_T = 2\sqrt{2\ln 2}\,\frac{\bar{v}}{w_0}$$ [29].

2.5.4. Pressure Broadening

The nature of pressure broadening can be understood classically by considering the molecule as a simple harmonic oscillator emitting an infinite train of sinusoidal electromagnetic radiation. Elastic collisions, from other molecules, introduce random phase changes in the otherwise continuous succession of radiation. The Fourier transform of the square of the amplitude represents the spectral line of such a system. This spectral line yields a Lorentzian function:

(Eqn. 44) $$I(\omega) = I_0 \frac{N\bar{v}\sigma_b}{(\omega-\omega_0-N\bar{v}\sigma_s)^2 + (N\bar{v}\sigma_b)^2}$$ [29];

where N is the number of particles, $\bar{v}$ is the average velocity of the gas, σ_s and σ_s are the cross-sections defined below:

(Eqn. 45) $$\sigma_s = 2\pi \int_0^\infty [\sin \eta(R)] R dR \qquad [29],$$

(Eqn. 46) $$\sigma_b = 2\pi \int_0^\infty [1 - \cos \eta(R)] R dR \qquad [29];$$

where η is the sum of all phase shifts.

If dampening by spontaneous emission of the oscillator and by inelastic collisions is included in this model ($\delta\omega_N$ and $\gamma_{elastic}$ respectively), the spectral intensity is:

(Eqn. 47) $$I(\omega) = I_0 \frac{(\frac{\delta\omega_N}{2} + \frac{\gamma_{inelastic}}{2} + N\bar{v}\sigma_b)^2}{(\omega - \omega_0 - N\bar{v}\sigma_s)^2 + (N\bar{v}\sigma_b)^2} \qquad [29].$$

The linewidth due to pressure broadening is typically determined experimentally by the formula:

(Eqn. 48) $$\delta\omega_P = \delta\omega_N + C_{ik}P \qquad [30];$$

where C_{ik} is the coefficient of collision-induced transition probability for a given transition from state i to k.

The values of C_{ik} have been found experimentally to have values between 1-60 MHz/Torr depending on the type of molecule and the temperature of the gas [30].

2.5.5. Saturation Power Broadening

Saturation of a transition by a spectrally narrow optical pump provides a certain velocity class within the state population to be depleted. The spectral profile of the saturation absorption dip is a Lorentzian function of the following form:

(Eqn. 49) $$I = \frac{\hbar\omega R\Delta N_0\left(\frac{P}{P_0}\right)(\gamma/2)^2}{(\omega-\omega_0)^2+(\gamma/2)^2(1+\frac{P}{P_0})}$$ [29];

where R is the relaxation rate, ΔN_0 is the population difference between levels, P is the power of the optical pump, P_0 is the saturation power, and γ is the combination of linewidths from natural, pressure, and transit time broadening.

The linewidth (γ_s) of this profile is:

(Eqn. 50) $$\gamma_s = \gamma\sqrt{1+\frac{P}{P_0}}$$ [29, 30].

The saturation power (P_0) is a parameter of the molecule being saturated and is of the following form:

(Eqn. 51) $$P_0 = \frac{\varepsilon_0 c\hbar^2\gamma^2 A}{2|\mu_{12}|^2}$$ [30];

where ε_0 is the permittivity of free space, A is the cross section of the optical pump, and μ_{12} is the dipole moment of the given transition.

2.5.6 Line Shifting Mechanisms

The interactions of a molecule with other molecules and radiation fields, not only cause broadening of the absorption lines, but also shifting of the line frequency. Among various mechanisms responsible for line shifts, two are typically the most prominent: pressure shift, due to collisions of molecules, and power shift, due to the Stark effect. These effects are quite evolved and it is difficult to relate the experimental results to the

fundamental parameter of the system without extensive theoretical work. A detailed theoretical analysis of pressure and power shifts of methane transitions has been accomplished by V. A. Alekseev, T. L. Andreeva, and I. I. Sobel'man [31], but aside from an intuitive understanding of these effects, no conclusions may be drawn for acetylene or ammonia.

3. Description of the Experimental System and Techniques

3.1. Laser Frequency Stabilization Systems

In **Figure 9** a schematic diagram of the laser frequency stabilization system apparatus is presented. At the heart of this system is an extended cavity diode laser (ECDL) (type: New Focus 6328 H). It is a commercial single-mode laser operating in a Littman-Metcalf configuration. The laser is tunable in the 1510-1570 nm range, can deliver up to 23 mW of output power, and its 50 ms linewidth is below 1 MHz. The second important part of the hardware is the Fabry-Perot interferometer, which consists of two highly reflecting mirrors attached to piezo-electric transducers glued to invar spacers. The whole interferometer is placed inside a vacuum chamber, which may be filled with various molecular absorbers. This apparatus provides stabilization for the laser frequency by two stages of control, each of which consists of a separate servo loop.

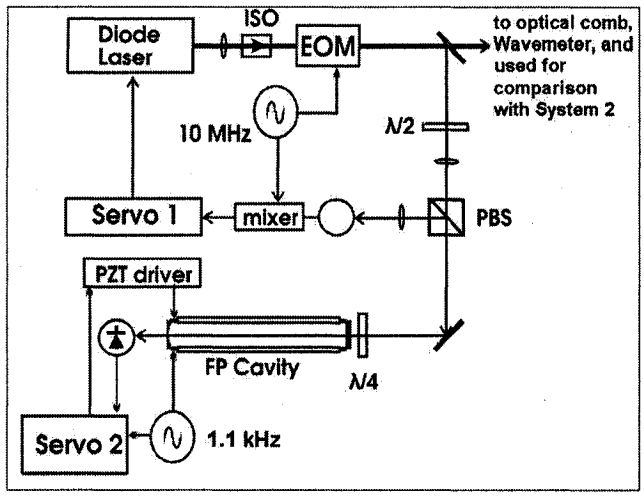

Figure 9: Schematic Diagram of the Frequency Stabilization Apparatus [11]. This figure shows the essential elements in the stabilization apparatus. This apparatus allows the laser frequency to be stabilized to the Fabry-Perot cavity and cavity stabilization to a saturated dip of the residing gas within. Where ISO is a Faraday isolator, EOM is an electro-optic modulator, PZT is a piezo-electric transducer, PBS is a polarized beam splitter, $\lambda/2$ is a half wave plate, and $\lambda/4$ is a quarter wave plate.

In the first stage of stabilization, the laser frequency is locked to the Fabry-Perot cavity using the Pound-Drever-Hall technique (see section **3.2**) [32]. Once this loop is closed, the laser operates as a slave with respect to the master Fabry-Perot cavity by Servo 1. Using the Pound-Drever-Hall technique in our apparatus permits reduction of noise on the laser and enables power build-up within the Fabry-Perot cavity. As a result, the saturation of weak transitions of a molecular gas within the cavity can be accomplished. At this stage, the frequency of the diode laser may only be tuned by changing the length of the interferometer, which is accomplished through the application of proper voltage on the piezo-electric transducers (PZT) of the Fabry-Perot cavity. The Fabry-Perot cavity transmission is consequently tuned to the molecular absorption of interest, when the second stage of the stabilization is engaged (Servo 2).

Servo 2 locks the Fabry-Perot transmission (and the laser locked to it) to the saturation feature of the molecular absorber by the third harmonic (or 3-f) locking technique.

In this work, two almost identical frequency-stabilized laser systems are used. These systems are designated System 1 and System 2 and have been developed and tested previously [11,16].

The optical system, Fabry-Perot interferometer, and both stabilization techniques are described in this chapter.

3.1.1. Description of System 1

The most important components of System 1 are illustrated on the diagram in **Figure 10**.

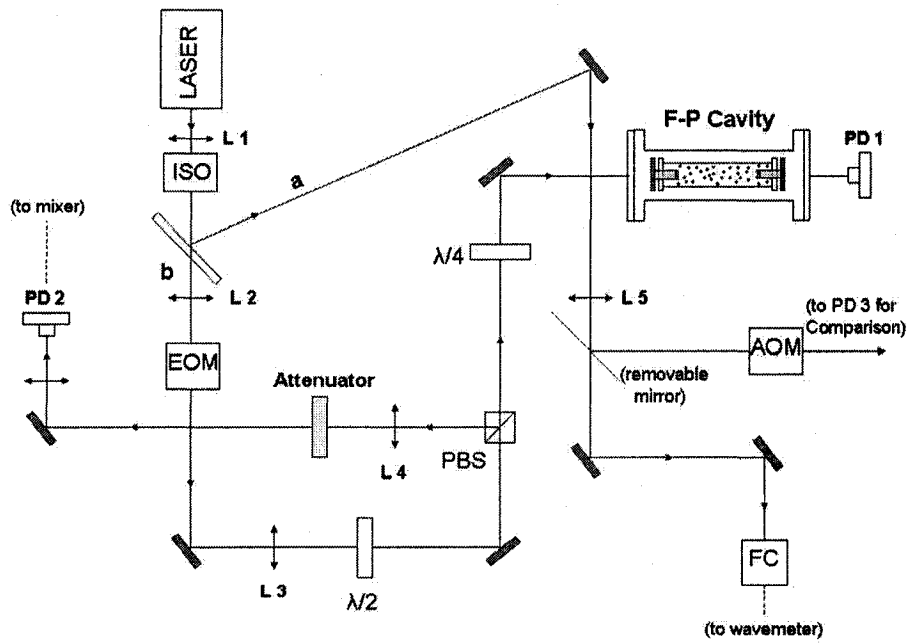

Figure 10: **Block diagram of System 1.** This figure illustrates the essential devices used in System 1 as well as the path of the beam, indicated by arrows. This system allows laser stabilization onto resonance of the Fabry-Perot cavity and cavity stabilization onto molecular transitions of the gas residing within. L1-L5 are lenses.

In this system, the beam exits the laser with carrier frequency, ω_0, and passes through a Faraday isolator (60 db), which prevents the reflected beam from re-entering the laser. The beam then passes through a beam splitter that splits the light into two parts, where 60% of the intensity is directed toward path "**b**" (as labeled in **Figure 10**). The remaining light following path "**a**" is led to a fibre coupler (FC). The fibre leads to a commercial traveling-mirror wavemeter (type: Burleigh, with 300 MHz resolution). An adjustable flip mirror is positioned in this path to intercept the beam. When this mirror is "flipped up", it reflects the light into an acousto-optic modulator (AOM), serving as a frequency shifter. The frequency of the "up-shifted" beam is then directed towards a fast photo-diode (PD 3 of System 2) for heterodyne beat detection (this technique is described later in this section). The second part of the beam, that follows path "**b**", passes through an electro-optic modulator (EOM). The EOM modulates the phase of the light, which introduces sidebands at frequencies of $\omega_0 \pm 10$ MHz. The modulated beam, now containing three frequency components, passes through a half wave plate ($\lambda/2$), which rotates the light's polarization by 90°. Following the half wave plate is a polarizing beam splitter (PBS) (with extinction ratio 1:500). After passing through the PBS, the light is sent through a quarter wave plate ($\lambda/4$), which rotates the polarization by 45°, and enters a Fabry-Perot cavity filled with a molecular gas (in our experiments, either NH_3, or C_2H_2). A proper lens arrangement is used to mode-match the laser beam profile to the TEM_{00} mode of the Fabry-Perot (F-P) cavity. A photo diode (PD 1) detects the light transmitted through the cavity while the reflected light, and the light leaking back from the interferometer, pass through the quarter wave plate again, acquiring polarization rotation of 90° with respect to the incoming beam. This allows the PBS to pick-off the reflected

light and direct it towards an attenuator and to a fast photo diode (PD 2). The detected signal is demodulated using the 10 MHz frequency from the EOM driver. This signal is then fed to a low-pass filter (of 1 MHz bandwidth) to isolate the portion of interest of the signal. The resulting signal provides the discriminator signal for the Pound-Drever-Hall stabilization.

3.1.2. Description of System 2

System 2 is employed as a stable frequency reference for that of System 1. The schematic diagram of System 2 is presented in **Figure 11**.

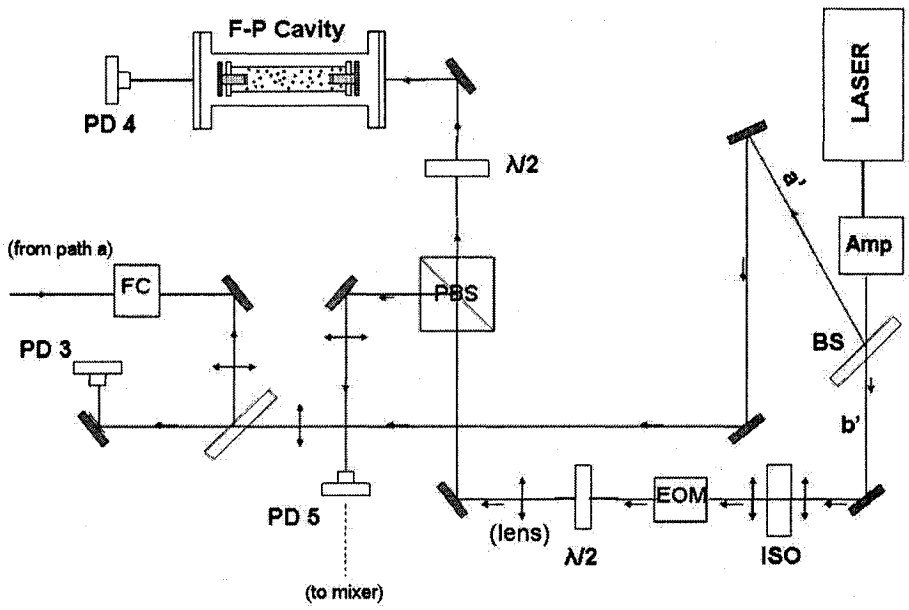

Figure 11: Block Diagram of System 2. Shown above are the essential devices used in design of System 2. System 2 is almost identical to System 1. The difference being that the EOM is modulating the laser beam at 12 MHz (instead of 10 MHz).

The laser output, in this system, is amplified by an Nortel Erbium-doped amplifier (AMP) and passes through a fibre coupler and then through a beam splitter. The beam

that follows path (a') is coupled with the exiting beam (along path a) from System 1. These beams are directed to a fast photo detector (PD 3) whose signal is fed to a frequency counter to determine the heterodyne beat. The portion of light that follows path (b') passes through an EOM modulated at 12 MHz. The rest of the arrangement for System 2 is similar to that of System 1.

3.1.3. Characterization of the Fabry-Perot Cavities

The System 1 Fabry-Perot cavity is enclosed in a vacuum chamber and it consists of two mirrors separated by an invar spacer with attached PZTs. The mirrors are attached to the PZTs and the PZTs are glued to the tilt plates of the Fabry-Perot cavity. The PZTs are cylinders of different lengths. The longer PZT is 2.54 cm, equipped with silver electrodes of 2 cm lengths, and the shorter is 1.50 cm with 0.9 cm long electrodes. Adjustment of the length of the cavity is achieved by applying voltage to the PZTs. The DC gains of the PZTs are 1.8 MHz/V and 0.7 MHz/V, respectively for the long and short. The shorter PZT is used to lock the cavity's resonance to the saturated absorption feature of a residing gas [11]. The radii of curvature of the two mirrors are: $R_1 = \infty$ and $R_2 = 1$ m. The reflectivity coefficients of each of these mirrors are 0.9928. R_1 serves as the input mirror for light and R_2 as the output.

The performance of the cavity was determined from measurements during operation. The free spectral range, FSR, of the cavity was measured to be 480 MHz and the linewidth, FWHM, of the resonant peaks was 1.1 MHz. This corresponded to a

finesse, $\Im$, of 436.5. The radius of the TEM_{00}, w_0, on the surface of the input mirror (R_1) was 0.47 mm.

The Fabry-Perot cavity used in System 2 was identical in design to that of System 1. Its parameters were as follows: the reflectivity of the mirrors equal 0.9954, FSR = 491.5 MHz, FWHM (of transmission) = 711 kHz, and $\Im = 691.4$. The PZT DC gain was 2 MHz/V for the long PZT, and 1.35 MHz/V for the short PZT.

3.2. Fundamentals of the Pound-Drever-Hall Technique

In many experiments involving commercial lasers it is necessary to operate with a stable frequency source. There are various methods to achieve frequency stabilization. Some of them rely on stabilizing laser systems using other stable sources, such as masers [33] or lasers [34]. Others make use of narrow atomic/molecular transitions and/or narrow resonances of stable Fabry-Perot interferometers. Among the latter, a particularly useful method is the Pound-Drever-Hall technique, which is one of the most powerful tools in frequency stabilization.

To understand the method qualitatively one may consider the experimental set-up presented in **Figure 12**.

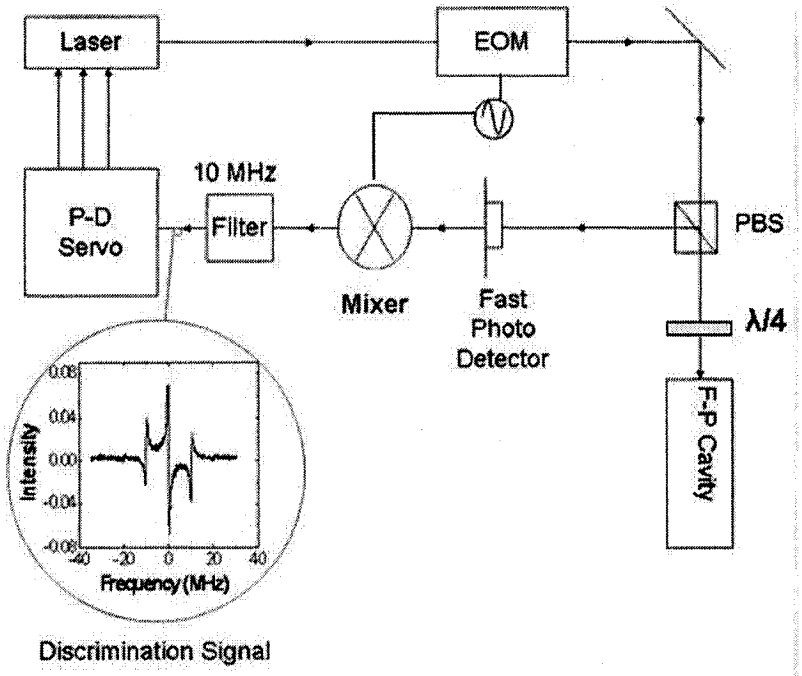

Figure 12: Block Diagram of a Pound-Drever-Hall Set-up. This technique employs a negative feedback loop to continually steer the laser frequency towards a resonant mode of the Fabry-Perot cavity [32].

The key part of this apparatus is the Fabry-Perot cavity that transmits light only for resonant frequencies of the cavity. The resonant frequencies are at integer numbers of the free spectral range, $FSR = c/2nL$, (where L is the length of the cavity, n is the index of refraction of the medium, and c is the speed of light [32]). The beam emerges from the laser with carrier frequency, ω_0, and is sent through an electric optic modulator (EOM). The EOM consists of a non-linear crystal oscillating at the frequency ω_{mod}. The EOM modulates the phase of the beam, which has the effect of introducing sidebands at $\omega_0 \pm \omega_{mod}$ to the frequency spectrum. After it leaves the EOM, the laser beam consists of 3 frequency components: the carrier frequency ω_0, and two sidebands at $(\omega_0+\omega_{mod})$ and $(\omega_0-\omega_{mod})$. The modulation frequency is set in such a way that ω_{mod} is outside of the cavity pass band. In our experiments, the modulation frequency is 10 MHz for System 1 and 12

MHz for System 2, where the FWHM of both cavities are roughly 1 MHz. The beam then passes through a polarizing beam splitter (PBS) and proceeds towards a quarter wave plate ($\lambda/4$). The quarter wave plate rotates the light's polarization by 45°. The Fabry-Perot cavity (F-P cavity) is located directly after the quarter wave plate in the optical path. The polarization of the reflected beam is rotated by 45° again as it is passed through the quarter wave plate a second time. This beam follows toward the polarizing beam splitter, which then directs it onto a fast photo detector. The light reflected from the F-P cavity contains frequencies at ω_0, $\omega_0 + \omega_{mod}$ and $\omega_0 - \omega_{mod}$. The fast photo diode detects the beat between each of these components: two beats of opposite phase and each at frequency ω_{mod}, which are produced from the interference of each sideband and the carrier signal; and one beat at frequency $2\omega_{mod}$, which is the beat produced from the interference of the two sidebands. A mixer, driven by a local oscillator, demodulates the detected signal to extract the signal at frequency ω_{mod}. The output from the mixer is sent through a low pass filter. This output is the Pound-Drever-Hall error signal (a measured error signal is shown in **Figure 12**). This signal has a strong dependence on the frequency of the laser beam with respect to the cavity's resonance. When the laser output beam is at a frequency equal to the resonance of the cavity, the signal has zero intensity. This signal is fed to the amplifier operating in a negative feedback loop to steer the laser frequency onto cavity resonance. A more detailed quantitative description of the Pound-Drever-Hall lock procedure is presented in **Appendix A**.

3.3. The 3-f Locking Technique

To lock the laser frequency to the saturated absorption lines, the 3-f lock (or third harmonic lock) technique is used. The schematic diagram of the 3-f servo-loop is presented in **Figure 13**.

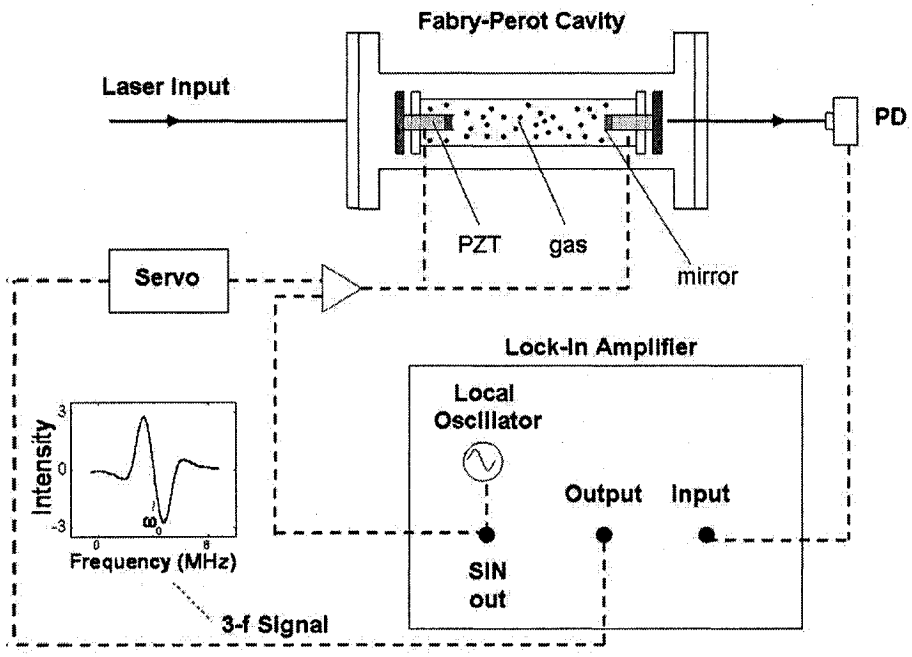

Figure 13: Apparatus for the 3-f Signal Detection. This set-up allows laser frequency stabilization on various saturated absorption dips of the gas within the Fabry-Perot cavity.

As the laser light passes through the Fabry-Perot cavity, the lock-in amplifier provides an oscillating signal to the PZTs to vary the cavity's resonance over a small frequency range about the saturated dip of the molecular absorber. A photo diode (PD) measures the cavity transmitted light. This signal is then demodulated by the lock-in amplifier at the 3-f frequency (a measured 3-f error signal is shown in **Figure 13**). This signal serves as an error signal for servo 2 and is responsible for locking the laser

frequency to the saturated absorption dip. The servo achieves frequency-stabilization on the saturated absorption dip by application of the correction voltage on the PZT of the cavity while working in a negative feedback loop with the error signal. Since the 3-f signal is precisely 0 at the frequency corresponding to the central point of the saturated absorption dip, the cavity's resonance stays centered on the dip and this, in turn, stabilizes the output laser frequency. A quantitative description of the 3f lock is offered in **Appendix B**.

3.4. Experimental Procedures

3.4.1. Activating the Pound-Drever-Hall Stabilization

In the process of implementing the Pound-Drever-Hall stabilization within our apparatus, the laser frequency is initially steered to the vicinity of the desired absorption line of the gas using the wavemeter as a guide. When the laser frequency is in vicinity of the absorption line, the signal transmission through the Fabry-Perot cavity has diminished intensity compared to neighboring resonator modes. This is verified during the experiment by ramping the laser frequency over several free spectral ranges of the cavity with a saw-tooth signal at 50 Hz and monitoring the transmitted light on the oscilloscope, a measured signal is presented in **Figure 14**.

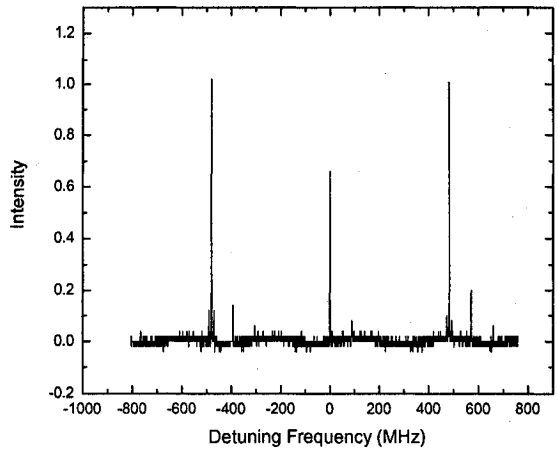

Figure 14: Diminished Transmission from the Fabry-Perot Cavity. This figure portrays the measured transmission from a Fabry-Perot cavity. The central peak has lower intensity than neighbouring peaks because it is in the vicinity of an absorption line of the residing gas inside. The plot was aquired by measuring the transmission of the cavity with 20 mTorr of $^{13}C_2H_2$ inside and laser output power set at 20 mW. The diminished peak is within the vicinity of the P(10) line.

The demodulated Pound-Drever-Hall discrimination signal is also observed on the oscilloscope to ensure that it has a background intensity of zero. If it is not zero, the half wave plate is adjusted to obtain this quality. The ramping of the signal is then turned off and servo gain is increased on the Pound-Drever servo amplifier. The laser frequency is slowly tuned to the cavity resonance by adjustment of the laser's PZT voltage control. As its frequency reaches the frequency of cavity resonance, the servo integrator switch is turned on to "grab" the laser frequency and keep it on resonance. Gain on the servo is then re-adjusted to minimize the noise on the discriminator signal. Once the laser is frequency-locked to the Fabry-Perot cavity it stays locked for several hours.
After the Pound-Drever-Hall lock is implemented, the cavity and the laser locked to it are slowly steered to the center of the absorption line; at which point, the second stage of stabilization is activated.

3.4.2. Activating the 3-f Frequency-Lock

After obtaining the Pound-Drever-Hall lock, the laser is locked to a mode of the Fabry-Perot cavity in the vicinity of maximum absorption of the gas that occupies the cavity. The laser frequency is then centered on this maximum absorption peak and the saturated absorption dip is observed on the oscilloscope. This is achieved by ramping the cavity's length with a saw-tooth signal at 1 Hz (5 MHz P-P) applied on the cavity's PZT. This allows the resonance of the cavity to sweep over nearby frequencies. The bias on the PZT driver for the cavity is then slowly adjusted until the saturated absorption dip can be observed on the oscilloscope (**Figure 15**). To confirm that this is the true absorption peak, the third harmonic is observed simultaneously from the lock-in monitor (**Figure 16**). The lock-in amplifier signal is used to dither the cavity over an amplitude of typically 1.8 MHz (peak to peak) at a frequency of 1 kHz to produce the 3-f signal. While the laser frequency is centered about the saturated dip, the PZT ramping is turned off. At this point the second servo is activated and the laser is then locked to the dip of the saturated absorption feature of the gas.

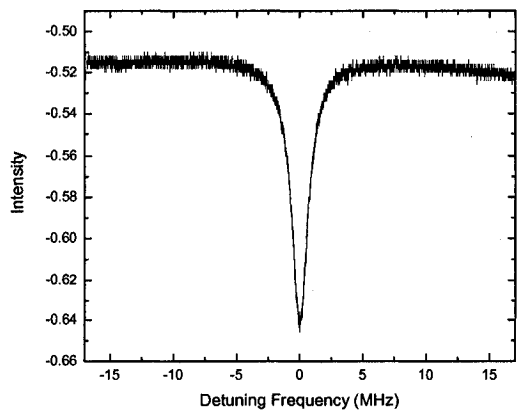

Figure 15: Measured Saturation Dip of $^{13}C_2H_2$. This profile illustrates the saturation dip of the P(16) absorption line of $^{13}C_2H_2$. Laser power was set at 14 mW and cavity pressure was 20 mTorr.

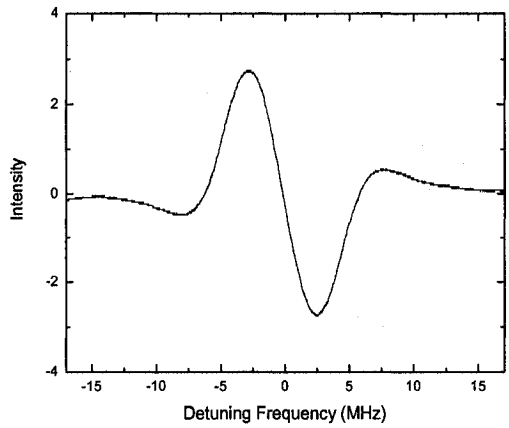

Figure 16: Measured Third Harmonic of $^{13}C_2H_2$. This profile illustrates the third harmonic signal from the saturation dip in **Figure 7**.

3.5. Frequency Comparison and Detection

In all of the experiments it is necessary to determine the frequency shift with respect to a stable frequency reference. This stable reference is provided by System 2, in which the laser is frequency-locked to the saturated dip of the same absorption line used in System 1. While parameters are being adjusted in System 1, the operating conditions of System 2 are kept constant. The laser output from System 1 and System 2 are combined on a beam splitter (BS) and directed onto a fast photo diode (PD) with a bandwidth of 1 600 MHz. A frequency counter is then used to measure the beat frequency between the two beams. The counter's output signal is fed to a local PC where the beat frequency is monitored and collected over time. This technique is known as the heterodyne beat technique. It allows one to measure the relative frequency of electromagnetic radiation throughout the spectrum. The experimental set-up for this procedure is shown in **Figure 17** below.

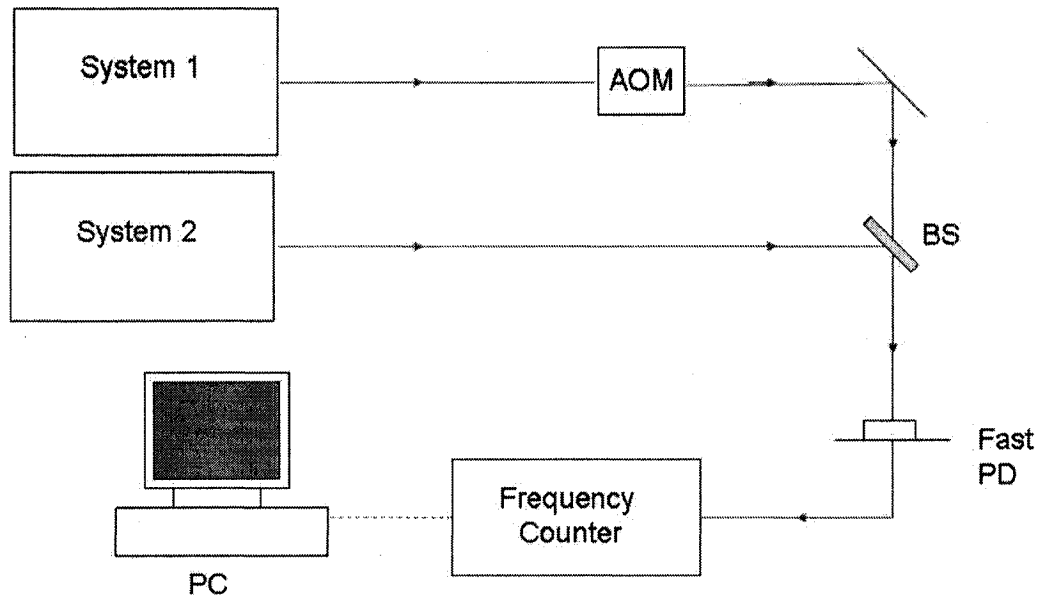

Figure 17: Heterodyne Beat Technique. In this technique, the laser beams from both systems 1 and 2 and combined on a photo detector. The photo detector distinguishes a beat and the frequency counter evaluates the frequency of this beat. This measurement is then fed to a local PC where a data acquisition program records the value.

To create a beat within a preferred range, an acousto-optic modulator (AOM) is employed to shift the frequency of System 1 by 80 MHz. This procedure is necessary for the following reason: if the two systems were both locked to identical absorption lines, essentially, they would have the same frequency. As a result, the frequency of the heterodyne beat would be at 0 Hz or very close. Suppose in such a case, that the beat frequency is 1/1000 Hz. To observe this beat, one would have to wait 1000 seconds (over 15 minutes!) to see a full period. This concept outlines the importance of having a frequency offset on one of the systems to facilitate quick data collection.

The heterodyne beat technique is employed in the experiments in this thesis measuring power shifting, pressure shifting, and modulation amplitude shifting.

3.6. Experimental Apparatus for Recording Doppler-Broadened Spectra of C_2H_2 and NH_3

The Doppler broadened spectra of C_2H_2 and NH_3 were investigated within the tuning range of our system's laser (1510 – 1560 nm) using a double-pass linear absorption cell apparatus. In this set-up (**Figure 18**), the output laser beam was directed through a half wave plate (rotating polarization by 90°) and toward a beam splitter. The beam splitter separated the original beam into two equal intensity beams. These beams are designated beam (1) and beam (2) on **Figure 18**. Beam (1) was incident onto a photo diode (PD 1) that measured the reference laser light intensity. Beam (2) was directed towards a quarter wave plate, where its polarization was rotated by 45°. This beam then entered the absorption cell. The cell was 1 m in length and filled with 10 Torr of either C_2H_2 or NH_3. A mirror placed at the end of the cell allowed the laser beam to reflect back and exit from the point of entry, also causing the light's effective travel length inside the absorbing material to be twice the length of the cell. Light was transmitted through the cell and passed through the quarter wave plate again and acquired another 45° rotation of polarization; as a result it was then picked-off by the beam splitter towards a second photo diode. This photo diode measured the intensity of the light after absorption.

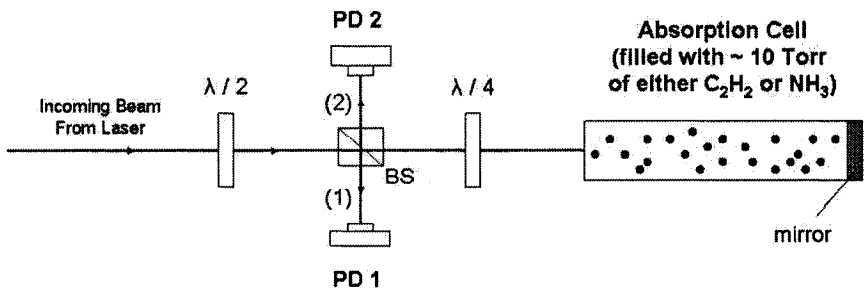

Figure 18: Schematic of the Apparatus for Doppler-Broadened Absorption. The system is designed to measure the intensity of the light before and after encountering the absorption cell.

Large sections of the absorption spectrum of NH_3 were recorded using the auto scan function on the New Focus laser of System 1. The scan feature allowed the ouput wavelength to be swept over 10 nm segments in 0.01 nm steps. Each scan took 3000 s. To improve the accuracy, the wavelength was monitored every 1 nm using the wavemeter.

For the purpose of investigating individual Doppler broadened lines, the above technique was too inaccurate. To obtain higher resolution spectra, the same apparatus **(Figure 18)** was used along with a signal generator that applied a saw-tooth signal to the laser's PZT to have the beam's frequency sweep over a range of only a few neighbouring absorption peaks of the spectrum (about 500 MHz). The profile was then obtained by recording the signals from the photo detectors with the data acquisition system. This short scan technique was used to produce small-range frequency scans over specific absorption lines of interest within the NH_3 spectrum, such as regions with high density of absorption lines where line assignments by wavemeter resulted in ambiguities.

4. Results and Discussion

4.1. Allan Deviation Plot of the Frequency Stabilizing Apparatus

One method of evaluating the stability of a frequency standard is to examine an Allan deviation plot. In this plot, the sample standard deviation, σ, is charted versus the averaging time of measurements.

Analysis of this plot allows one to characterize the noise of the system. Several sources of noise in the system may include: thermal drifts, acoustic vibrations, local electronic interference, flicker noise, white noise, and shot noise. The Allan deviation plot may also be used to determine an optimum averaging time for a measurement, as well as its limits.

The Allan deviation plot for our frequency-stabilized system was produced by operating the system for a run-time of over 1800 s while the lasers frequencies of System 1 and System 2 were each locked to the saturation dip of the $\nu_1 + \nu_3$ P(16) line of $^{13}C_2H_2$. During this time, measurements of the 1 second-mean beat frequency were made by the frequency counter and collected with the data acquisition program. A plot of the beat frequency over time is illustrated in **Figure 19**.

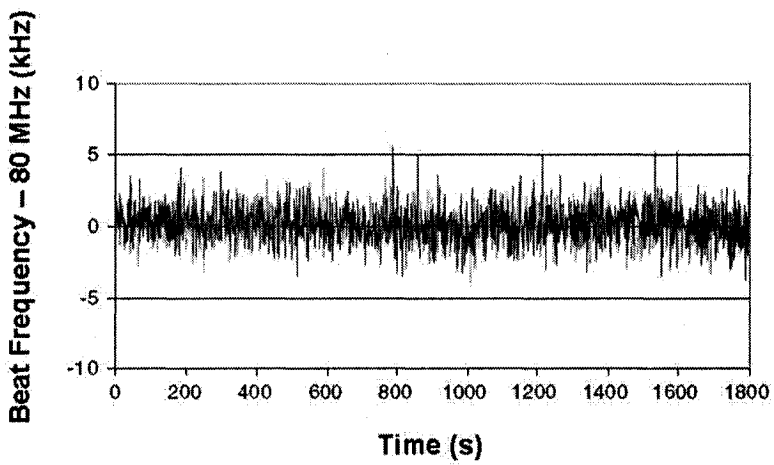

Figure 19: Stabilization Performance while Locked to P(16) $^{13}C_2H_2$ [11]. The lasers within system 1 and 2 were both locked to the saturated absorption feature of P(16) $^{13}C_2H_2$ with each Fabry-Perot cavity filled with 20 mTorr of acetylene. The output power of the laser in system 1 was set at 19 mW and the laser of system 2 to 40 mW. The beat frequency was measured during the lock over a period of 1800 s.

A histogram of the data set of beat frequencies in **Figure 19** is plotted in **Figure 20**.

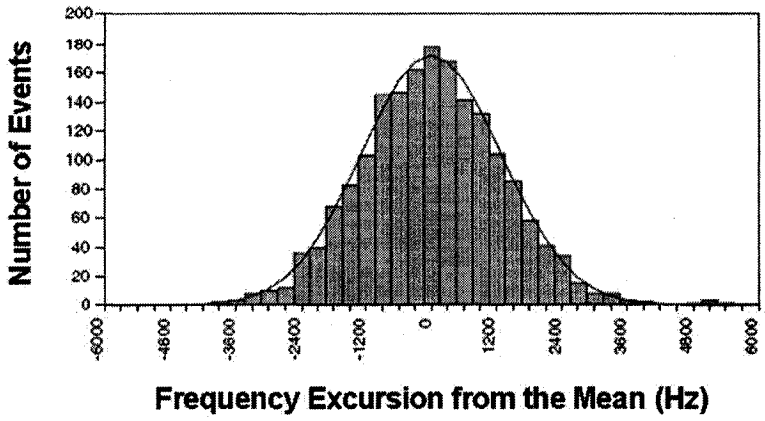

Figure 20: A Histogram of the Beat Frequency Value for the P(16) Lock to $^{13}C_2H_2$ [11]. In this plot, the beat frequency values are divided into bins of 300 Hz width. The mean value is 80 000 111 Hz with a standard deviation, σ, of 1 300 Hz.

The solid line in **Figure 20** is a Gaussian profile. This function illustrates the normal distribution of the beat frequency measurements.

Ideally to obtain an Allan deviation plot, the experiment should be performed several times with varied averaging times of the frequency counter for each trial. However, for counters with sufficiently small dead-time, the Allan deviation plot may be produced from a single experimental run by progressive averaging. In this given trial, the gate of the frequency counter was set at 1 s. The sample standard deviation of the beat frequency was calculated from the 1800 values obtained. A gate-time of 2 s was then simulated by averaging the original data set of measurements over 2 second intervals, producing a new set of data of roughly 900 values. The sample standard deviation was then calculated for this data set. This value of sample standard deviation represented the sample standard deviation of the beat frequency with a 2 s averaging time (or measuring the beat frequency with the frequency counter's bin-time set at 2 s). A gate-time of 4 s

was simulated by averaging the data set of the "2 s bin time" in intervals of 4 s. This technique was repeated to produce "bin-times" between 1 and 500 seconds.

The Allan deviation plot for the frequency lock to P(16) $^{13}C_2H_2$ is presented in **Figure 21**.

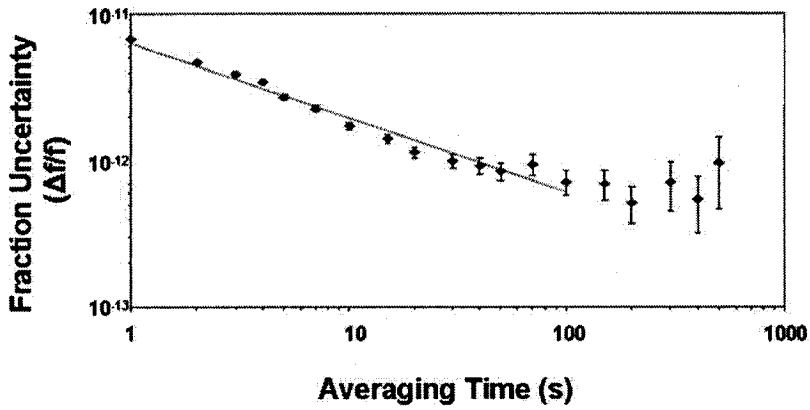

Figure 21: Allan Deviation Plot of the Frequency Lock to P(16) $^{13}C_2H_2$ [11]. The sample standard deviation was plotted against bin-time (or averaging time).

The Allan deviation plot produced (**Figure 21**) indicates that the slope levels-off adequately between 50 and 200 seconds of sampling time. This means that the deviation taken in this range would be close to its minimum value. After such times, stability of the system would not improve over longer averaging times. For this reason, measurements of beat frequency taken during frequency stabilization experiments (i.e. power shift, pressure shift, and modulation shift experiments) were performed over a designated sampling time of 60 to 100 s, which resided within the range of low-valued slope of the Allan deviation plot. This allowed one to collect data over a reasonable period of time considering the number of measurements that were accumulated.

The stability of the frequency-stabilized system, while locked to the P(16) transition of the $\nu_1 + \nu_3$ band of $^{13}C_2H_2$, has been determined by examination of the Allan deviation plot. The measured result of this plot has shown the system to reach a stability of 6×10^{-13}

for an averaging time of 100 seconds. The stability of this system is comparable to the reported stability of acetylene based frequency-standards employed at the National Institues of Advanced Industrial Science and Technology (AIST) and the National Physics Laboratory (NPL), which have recently reported values of stability of 1×10^{-13} over an averaging time of 10 000 seconds [35] and 1.6×10^{-13} over an averaging time of 100 seconds [36], respectively.

4.2. Intracavity Power Shift on Absorption Lines of C_2H_2

The Stark effect is a perturbation that causes shifting of energy levels due to the presence of an electric field. This results in the shift of an absorption line of a molecule. When the laser field itself is the source of perturbation, the effect is known as the AC Stark effect.

By changing the intracavity power, in one of the laser systems, while recording the beat-note frequency, we are able to measure direct effects of the AC Stark effect on molecular transition frequencies. Typically, power shift measurements were taken at 20 mTorr of pressure in both systems. However, in the case of strong absorption, it was required to use less gas to observe sufficient transmission. During experiments, the output power from the laser in System 2 was held constant, while the output power of the laser in System 1 was adjusted in regular intervals (typically in 2 mW intervals) from 8 mW to 23 mW. This corresponded to 4 -10 mW of power delivered to the Fabry-Perot cavity, out of which about 50% penetrated into the interferometer. The power enhancement inside the cavity produced between 30-300 mW of intracavity power for various absorption lines of acetylene. At each set value of power, a beat-note frequency

was recorded for 100 seconds. **Figure 22** illustrates a typical plot of the beat frequency versus time while output power was adjusted for the $\nu_1+\nu_3$ P(10) line of $^{13}C_2H_2$.

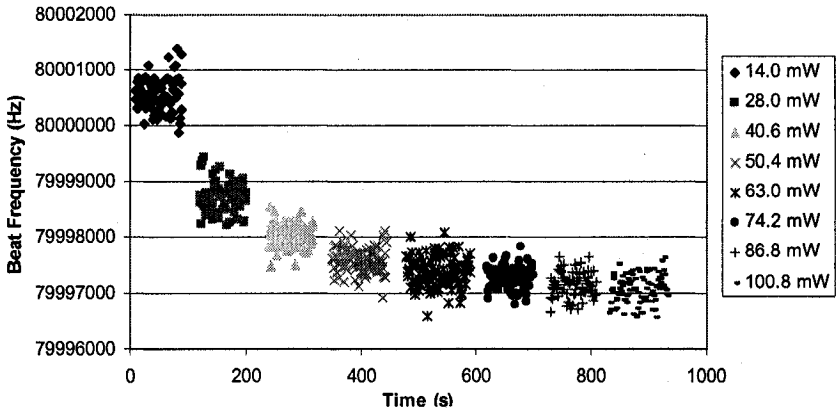

Figure 22: Power Shift of P(10) $^{13}C_2H_2$ over Time. This figure shows the plot of beat frequency vs time throughout varying intracavity power from 14 - 28 mW. Both systems were locked to line P(10) of $^{13}C_2H_2$ with the cavity in System 1 filled with 20 mtorr of acetylene. These power settings are left running for a period between 60-100 s.

The values of the beat frequency within this plot (**Figure 22**) decrease with time as the strength of intracavity power increases. A plot of the mean beat frequency versus intracavity power is presented in **Figure 23**.

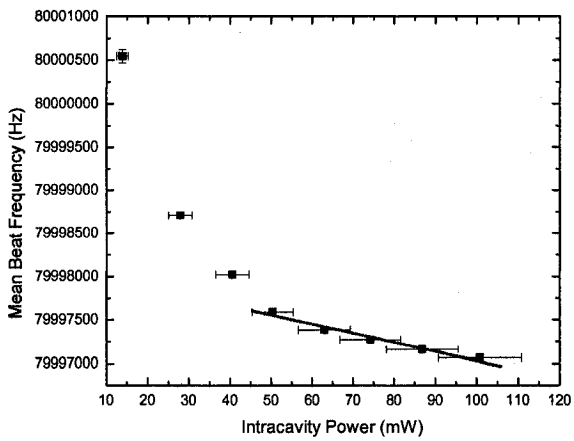

Figure 23: Power Shift of $^{13}C_2H_2$ Line P(10). The 100 s mean value of beat frequency is plotted against the value of intracavity power. The uncertainty budget on the mean beat frequency is the standard deviation of the mean. Uncertainty for intracavity power is 10% of the intracavity power value.

The mean value of the beat frequency in the 100 second interval was designated as the actual value of frequency for the existing settings. This value may be reported with an associated uncertainty of the standard deviation of the mean within the time interval of the current setting (as seen in **Figure 23**).

Using linear regression analysis, the slope of the power shift plot for the P(10) line of $^{13}C_2H_2$ **(Figure 23)** was determined to be -10.5 ± 0.8 Hz/mW. Note that the three points of lowest values of intracavity power are not included in the linear fit. This is because it is believed that the frequency-stabilized apparatus is outside of the optimum range of performance and that shifts within this low power region are artifacts of the system, not due to the Stark effect.

For optimum accuracy on the evaluation of slope for intracavity power shifting, experiments were repeated several times for a given absorption line while adjusting the intracavity power throughout the same range. From each trial, a linear fit was produced and the value of the slope was calculated. The reported value of the intracavity power shift is based on a weighted average of the inverse square of error on the determined slopes. The slope values for power shifting have been measured for 6 lines of $^{13}C_2H_2$ and 5 lines of $^{12}C_2H_2$ within the P and R branches of the $\nu_1+\nu_3$ combination band. These values along with their corresponding uncertainty and range of intracavity power are listed in **Table 2** and **Table 3**.

Table 2: Power Shift Slopes of $^{13}C_2H_2$

$^{13}C_2H_2$ Line	Power Range (mW)	Slope (Hz/mW)	Uncertainty (Hz/mW)
P(10)	40-100	-11.9	0.8
P(11)	56-126	-21.5	1.1
P(14)	40-83	-19.1	1.6
P(15)	65-180	-19.8	1.4
P(16)	56-180	-12.8	0.5
P(20)	75-212	-8.8	0.7

Table 3: Power Shift Slopes of $^{12}C_2H_2$

$^{12}C_2H_2$ Line	Power Range (mW)	Slope (Hz/mW)	Uncertainty (Hz/mW)
P(3)	46-110	-16.0	0.9
P(4)	96-292	-13.8	1.0
P(13)	46-87	-200	15.0
P(14)	133-291	-29.6	2.3
R(8)	40-65	-110	7.0

In many of the plots of beat frequency versus intracavity power, points of low value of intracavity power were not included for the linear fit. This was because a common non-linear trend of frequency shifts, within the low intracavity power region (less than 40 mW), was observed for the absorption lines in this study. For such low strengths of power, the transmitted light signal is significantly lower. This, in turn, affects the signal to noise ratio (SNR) of the 3f error signal controlling the stabilization lock to the saturated dip. For this reason, the behaviour of frequency shifts for low intracavity power was attributed to be an artifact of the servo stabilization system. To limit our investigation to frequency shifts due to power shifting, we have focused our analysis on beat frequency measurements with intracavity power above 40 mW, where no apparatus effects were observed.

The slope values for intracavity power shift on $^{13}C_2H_2$ range between -21.5 and -8.8 Hz/mW for 6 absorption lines within the P-branch of this molecule. These values are reported within an uncertainty of 0.5-1.6 Hz/mW. These results are in agreement with the measured power shift slope on the P(16) line of this molecule that was obtained earlier at NRC [11]. The result from this previous study was -11.4 ± 0.6 Hz/mW, compared to our value of this line: -12.8 ± 0.5 Hz/mW.

The intracavity power shift slope was measured for 5 lines of $^{12}C_2H_2$. Overall, good quality frequency-locks were obtained for lines: P(3), P(4), and P(14). The slope values of power shifts range from -29.6 to -13.8 Hz/mW with uncertainty ranging from 0.9 to 2.3 Hz/mW (**Table 3**). These results are of the same order of magnitude as the values of power shift for absorption lines of $^{13}C_2H_2$ (**Table 2**), which is to be expected. However, the frequency locks that were obtained for lines P(13) and R(8), to measure the

power shift effect, were of poor quality, as can be seen by the larger extent of uncertainty associated with these measurements, 15.0 Hz/mW and 7.0 Hz/mW respectively. The poor quality of lock was attributed to the high absorption strength of these two lines which decreased the reflected light from the Fabry-Perot cavity and consequently deteriorated the error signal and stability of the Pound-Drever-Hall lock.

4.3. Pressure Shift on Absorption Lines of C_2H_2

The effects of variation of acetylene pressure on the frequency of absorption lines were investigated by collecting measurements of the beat frequency between the System 1 and System 2 lasers while each system's laser frequency was locked to a specific absorption line of the gas. The pressure and power, and all other operating parameters of System 2 were held constant throughout these measurements. Within System 1, all of the parameters except pressure were held constant, including the output power of the laser. However, due to the change of acetylene density (associated with the change of pressure), the intracavity power would, nevertheless, change. To be able to subtract this effect, intracavity power was closely monitored during the experiments. The pressure shifts were investigated by adjusting the pressure in the range of 5 and 50 mTorr. As with experiments measuring power shifts, pressures of acetylene were held constant for about 100 seconds while the beat frequency was measured. A typical plot of beat frequency versus time, while adjusting pressure, is presented in **Figure 24.**

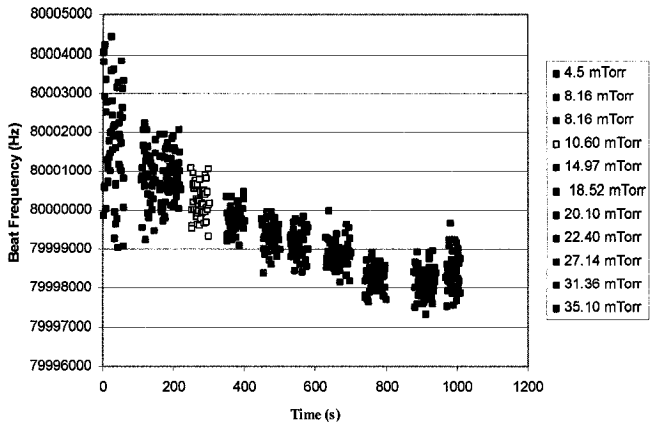

Figure 24: Pressure Shifts of the P(11) line of $^{13}C_2H_2$. This figure shows a plot of the beat frequency between System 1 and System 2 while locked to the P(11) transition of $^{13}C_2H_2$. Pressure was increased from 4 to 35 mTorr during the lock. Laser output power of System 1 was set at 12.0 mW.

A plot of the mean beat frequency versus cavity pressure, while locked to the P(11) transition of $^{13}C_2H_2$, is illustrated in **Figure 25.**

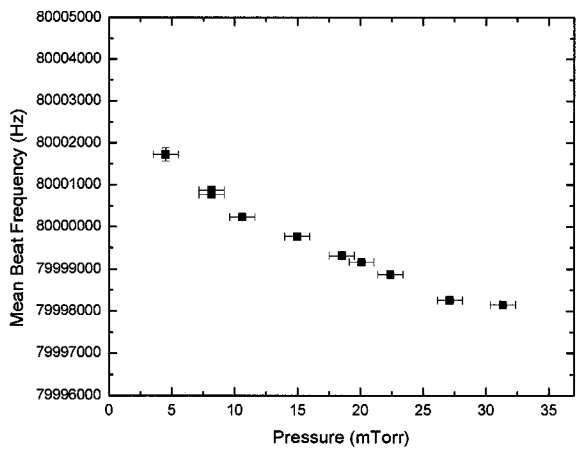

Figure 25: Line Shifting of P(11) $^{13}C_2H_2$ due to Pressure and Power Variation. This plot shows the mean beat frequency versus pressure between a range of 4 and 35 mTorr. Measurements were taken while adjusting pressure of acetylene with constant laser output power of 12 mW. Intracavity power was also affected by the increase of acetylene and shifts due to power variation are not yet corrected in this figure.

The budget of uncertainty of the frequency measurement, at a given pressure, is denoted by the sample standard deviation. The uncertainty of the pressure measurement is ±1 mTorr.

To isolate the effect of frequency shifting due to pressure variation, the effect of power shifting was subtracted from these measurements. This was accomplished by monitoring the change in intracavity power between each point. For correction of this factor the slope of power shift of this absorption line, P(11) of $^{13}C_2H_2$, was required. The experimentally determined slope value for power shifting of this line was -21.5 ± 1.1 Hz/mTorr. Using this value, shifts due to changes of intracavity power between each value of pressure were subtracted using the power shift slope of this absorption line. Due to the error on the power slope measurement, there was additional uncertainty added to the error bars of these measurements. The amount of added error, for this example, was 5.1% (the ratio of error to measurement for the power shift slope: $\frac{1.1}{21.5}$) of the subtracted frequency value from power shifting. A new plot was then produced that illustrated line shifting solely due to pressure shifting (**Figure 26**).

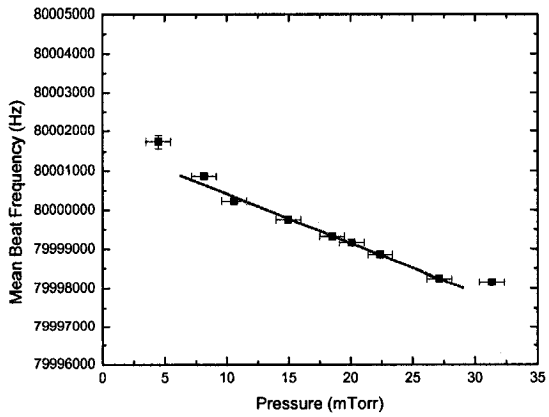

Figure 26: Pressure Shift of P(11) $^{13}C_2H_2$. Effects of power shifting have been subtracted, and the appropriate amount of error added. The slope of the fitted line for this plot is 126 ± 4.3 Hz/mTorr.

The linear fit for the plot in **Figure 26** neglects a point from the lowest pressures as well as a point at the highest pressure. This is because the frequency-lock is believed to be outside the range of optimum performance.

Measurements of pressure shifts were performed numerous times for each line while adjusting pressure over the range of roughly 5-40 mTorr. The effects of power shifting were subtracted for each set of data and the slope of pressure shifting was calculated. A weighted average of all the measured slopes was taken for each absorption line based on the inverse square of error. **Table 4** lists the pressure shift values and uncertainties for 4 absorption lines of $^{13}C_2H_2$ within the P branch of the $\nu_1+\nu_3$ combination band.

Table 4: Pressure Shift Slopes of $^{13}C_2H_2$

$^{13}C_2H_2$ Line	**Pressure Range (mTorr)**	**Slope (Hz/mTorr)**	**Uncertainty (Hz/mTorr)**
P(11)	5-50	176	6
P(14)	20-50	433	14
P(15)	10-50	82	8
P(20)	15-50	79	10

As with power shift, there was an optimum range of pressure that provided quality stabilization to the saturated dip of a specific line. This range varied for different absorption lines, but was typically within the 5 – 30 mTorr region. Outside of this region it was believed that the stabilizing lock deteriorated and frequency shifts arose due to

artifacts of the servo. Linear fits within plots of beat frequency versus pressure were also confined to points within this region.

The results for pressure shifts of the P(11), P(15), and P(20) absorption lines of $^{13}C_2H_2$ (**Table 4**) were generally of the same magnitude, in the range of -176 to -79 Hz/mTorr within an uncertainty range of 6 – 10 Hz/mTorr. Line P(14) demonstrated stronger pressure dependence: 433 ± 14 Hz/mTorr. These values are overall comparable, with the exception of the P(14) line, to results obtained by other measurement institutes within the uncertainty budget. Pressure shift of the P(16) transition was measured, by other groups, at similar conditions, to be: -230 ± 20 Hz/mTorr [11], -200 ± 70 Hz/mTorr [37], and -40 ± 133 Hz/mTorr [38]. Although this particular line was not used in our pressure shift experiments, we can generally expect that the value of the pressure shift is the same order.

4.4. Modulation Amplitude Shift on Absorption Lines of C_2H_2

The modulation amplitude is a parameter of the system that reports the amount of dithering of the cavity's resonance over the saturated absorption feature of the gas. To obtain the 3-f discrimination signal, the resonance of the cavity needs to be continually modulated for the lock-in amplifier to "see" the saturated absorption feature. The frequency span that the resonance is swept over is the modulation amplitude. The 3-f discrimination signal, which is obtained from dithering, is fed to the stabilizing servo to frequency-lock to the saturated absorption dip feature. The effects of modulation on the

lock-point are related to the perturbation of the given transition by nearby energy states. These local states may introduce asymmetries to the lineshape [39]. By changing the depth of modulation, one changes the "amount of asymmetry" that affects the line and line centre.

The value of modulation amplitude of the operating system was investigated under variation over a range between 1.80 and 9.43 MHz (peak-to-peak) while keeping all other parameters, such as intracavity power and cavity pressure, constant. This modulation was adjusted regularly by 0.9 MHz intervals every 100 seconds while the heterodyne beat frequency was recorded.

Figure 27 illustrates a typical plot of amplitude modulation variation for the plot of mean beat frequency versus modulation amplitude for the P(13) line of $^{12}C_2H_2$.

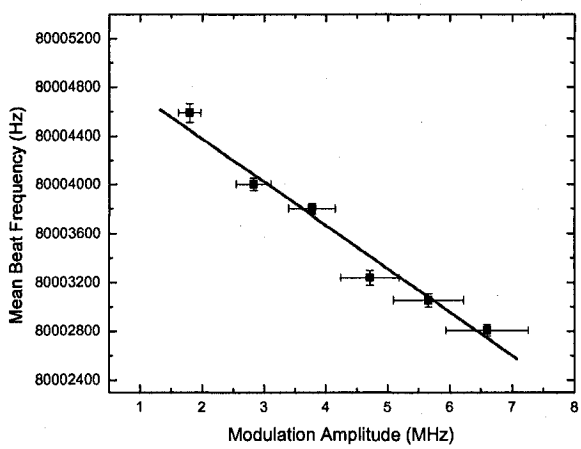

Figure 27: Modulation Amplitude Shift for P(3) $^{12}C_2H_2$. Measurements of this plot were taken with cavity pressures of 21.5 mTorr and 22.0 mTorr and laser output powers set at 20 mW and 40 mW for system 1 and system 2 respectively. The slope of the fitted line was -354 ± 14 Hz/MHz

Measurements of modulation amplitude shifts were collected for 4 absorption lines of $^{12}C_2H_2$ over a range of amplitude modulation from 1.80 and 9.43 MHz. Several

values of shifting were measured for a given transition and the reported value of the modulation amplitude shift was based on a weighted average of the inverse square of error of the measurement. **Table 5** lists the values of frequency shifts due to amplitude modulation for 4 absorption lines of $^{12}C_2H_2$ within the P branch of the $\nu_1+\nu_3$ combination band.

Table 5: Modulation Amplitude Shift Slopes of $^{12}C_2H_2$

$^{12}C_2H_2$ Line	Modulation Range (MHz)	Slope (Hz/MHz)	Uncertainty (Hz/MHz)
P(3)	2-7	-437	24
P(4)	1-5	-360	76
P(13)	3.5-7.5	-1063	61
P(14)	4-9	-1284	50

Line shifting due to variation of modulation amplitude was measured in our experiments on various absorption lines of $^{12}C_2H_2$. Previous studies performed by several metrology institutes [11, 36, 37, 38, 40] have focused on the $^{13}C_2H_2$ molecule. Their results may still be used for comparison, as well as to illustrate the magnitude of frequency shifts due to variation of amplitude modulation.

The measured modulation amplitude shifts in $^{12}C_2H_2$, from our study (**Table 5**), range from -1.3 to -0.5 kHz/MHz, with uncertainty in the range of 24 – 76 Hz/MHz for lines: P(3), P(4), P(13), and P(14). Results by other groups have reported the frequency shift of the P(16) line for $^{13}C_2H_2$ to be as follows: -4.7 ± 0.3 kHz/MHz [11] and 0 ± 1 kHz/MHz [38]. The amplitude modulation shift for line P(10) $^{13}C_2H_2$ was reported to be

– 1.3 kHz/MHz [36]. These results of 0 ± 1 kHz/MHz [38] and -1.3 kHz/MHz [36] do fit within our measured range of amplitude modulation shifts.

4.5. Discovery of the Saturated Absorption in NH_3

Due to interest in new frequency markers for telecommunication references, several specific absorption peaks of the NH_3 spectrum were investigated at high resolution. For some of these lines saturation was achieved. The absolute frequencies of these lines were measured using a $Cr^{44}YAG$ frequency chain and are listed in **Table 6** along with the approximate wavelength of these lines, as measured by the wavemeter.

Table 6: Selected Wavelengths and Measured Absolute Frequencies

Wavelength (nm) ± 0.005 nm	Measured Absolute Frequency (Hz)
1512.24	198 244 327 065 000
1541.65	195 731 505 670 000
1554.06	192 910 048 789 000

The absorption line profile, saturation dip, and the 3-f signal for these lines are presented in **Figures 28-35**.

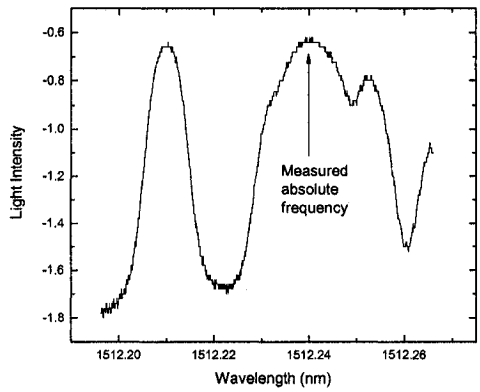

Figure 28: Doppler Broadened Absorption Lines of NH_3 in the Vicinity of 1512.24 nm. This profile was recorded by monitoring the laser light intensity through an absorption cell filled with 10 Torr of NH_3 while scanning the laser frequency.

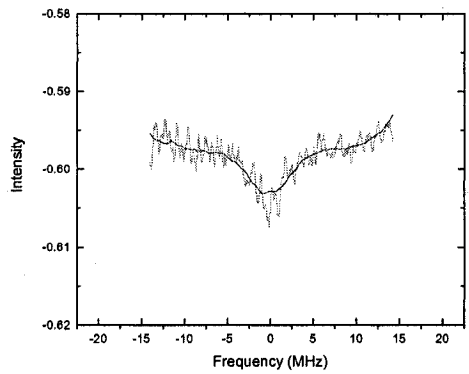

Figure 29: Saturated Dip of the Absorption Peak of NH_3 at 1512.24 nm. This figure shows the profile of a saturated dip and its averaged plot in solid (averaged over 300 point intervals). This profile was measured with cavity pressure of 20 mTorr of NH_3 and laser output power of 20 mW.

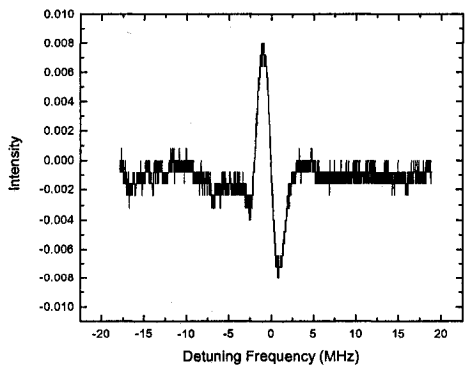

Figure 30: 3-f Signal from the Saturated Dip of NH_3 at 1512.24 nm. This profile is the third harmonic error signal from the saturated dip profile in **Figure 20**. Notice the poor signal to noise ratio due to the very weak saturated dip profile.

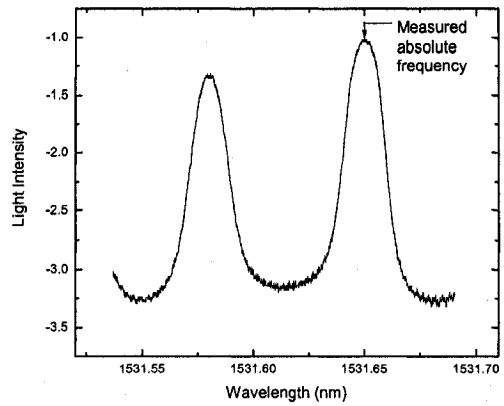

Figure 31: Doppler Broadened Absorption Lines of NH_3 in the Vicinity of 1531.65 nm. This profile was recorded by monitoring the laser light intensity through an absorption cell filled with 10 Torr of NH_3 while dithering the laser frequency.

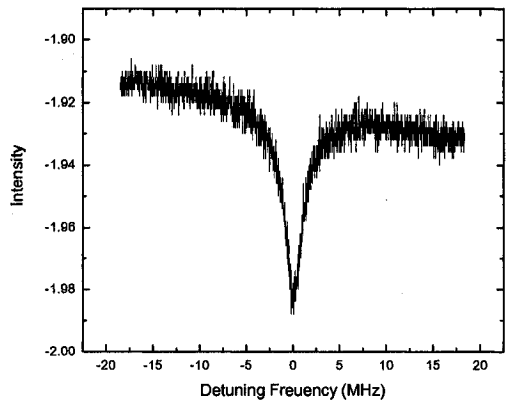

Figure 32: Saturated Dip of the Absorption Peak of NH_3 at 1531.65 nm. This profile was measured with cavity pressure at 20 mTorr and laser output power at 20 mW.

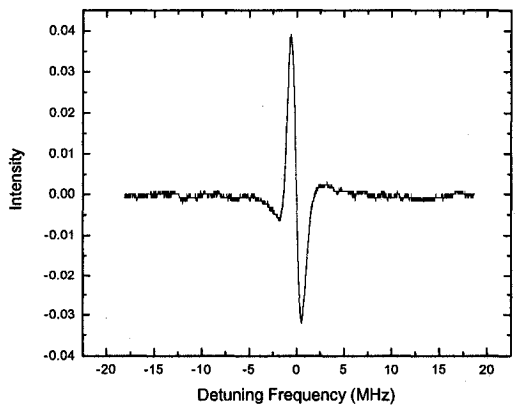

Figure 33: 3-f Signal from the Saturated Dip of NH_3 at 1531.65 nm. This profile shows the demodulated error signal produced from the saturated dip in **Figure 21**.

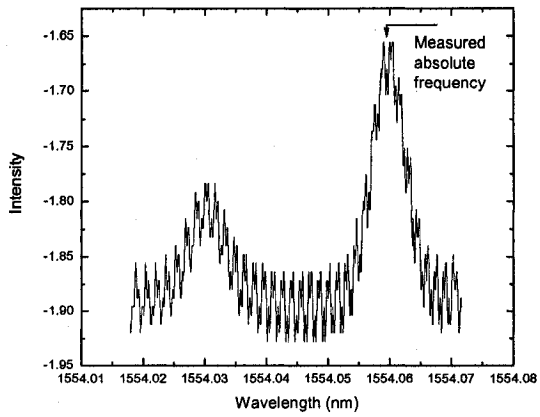

Figure 34: Doppler Broadened Absorption Lines of NH_3 in the Vicinity of 1554.06 nm. This profile was recorded by monitoring the laser light intensity through an absorption cell filled with 10 Torr of NH_3 while dithering the laser frequency.

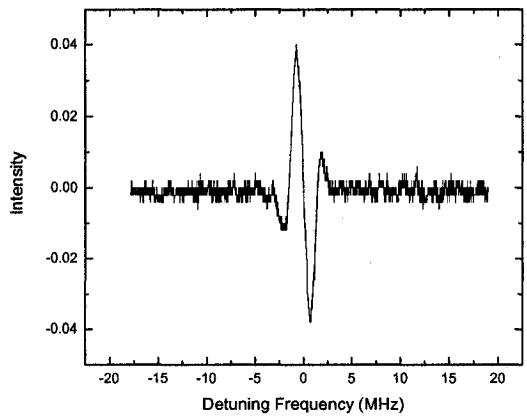

Figure 35: 3-f Signal of the Saturated Dip of NH_3 at 1554.06 nm. This profile shows the third harmonic signal from the absorption dip at 1554.06 nm. The absorption dip of this line is not shown in any figure because it is indistinguishable from the noise (similar to **Figure 29**).

Figures 28, **31**, and **34** present the NH_3 spectrum in the vicinity of three particular absorption lines. These lines were chosen to demonstrate the possibilities of using NH_3 for optical metrology. Saturation of these lines has also been achieved for the first time

within our apparatus. The saturated absorption dips of these lines are shown in **Figures 29** and **32**. The saturated dip in **Figure 29** is not resolved very well, due to weaker absorption (as can be seen in **Figure 28**), although the saturated absorption dip in **Figure 32** is distinguished with much improved quality because the absorption line is stronger (**Figure 31**). The 3-f signals of these saturated absorption dip are shown in **Figures 30, 33**, and **35**. As expected, the absorption line at 1531.65 nm (**Figure 31**) produces the 3-f signal with the best SNR.

A frequency lock onto several absorption lines of NH_3, including the three studied in depth, was also attempted, although, the measurements of parameter shifts could not be reported with a substantial degree of accuracy. Frequency locks to this molecule tended to drift in frequency on the order of 30 kHz. Work on a new electronic system is required before reliable studies of these effects in NH_3 may be continued.

4.6. Measurements of the Saturation Power and Linewidth from the Power Broadening of Selected Lines for $^{13}C_2H_2$, $^{12}C_2H_2$, and NH_3

The effect of power on the saturated absorption linewidth was studied for $^{13}C_2H_2$, $^{12}C_2H_2$, and NH_3. This was accomplished by filling a Fabry-Perot cavity with one of the gases in question and saturating a particular Doppler-free transition of the molecule. Profiles of the saturated dip features were obtained by measuring the transmitted light of the cavity while the laser frequency was dithered over a corresponding frequency range of 33.8 MHz.

Investigating the line broadening of these profiles as a function of power allows one to determine the saturation power and the natural line width of the absorption line. The predicted relation between linewidth, γ, and electric field power inside the cavity, P, is given by **Eqn. 50**.

An estimation of the line width, γ, and the saturation power, P_0, was obtained for several absorption lines of $^{13}C_2H_2$, $^{12}C_2H_2$ and NH_3 by measuring the FWHM of the saturation dip for various values of intracavity power and constant pressure. The FWHM of the saturation dip, and its uncertainty, were determined by fitting a Lorentz function to this feature. The square of the full width at half maximum, $(FWHM)^2$, of the saturated dip was then plotted against intracavity power. The error on the intrapower values was allocated its usually 10% of measurements and the error on the value of $(FWHM)^2$ was obtained using the propagation of error formula:

(Eqn. 52) $$\Delta x = \sqrt{\sum_i (\Delta x_i)^2 (\frac{\partial x}{\partial x_i})^2}\ ;$$

where x is a function of $(x_1, x_2, x_3 \ldots x_n)$, Δx is the uncertainty of x, and Δx_i is the uncertainty of the variable x_i.

A linear regression fit of this plot was then used to obtain the value of the slope and intercept. The value of the intercept determined the parameter γ^2 and the slope determined the parameter $\frac{\gamma^2}{P_0}$. The values of line width, γ, and saturation power were then calculated and uncertainty was determined using the error formula (**Eqn. 52**). Profiles of the saturated absorption line at selected values of intracavity powers for $^{13}C_2H_2$ are presented in **Figure 36**. A Lorentzian fit of this profile is shown in **Figure 37**.

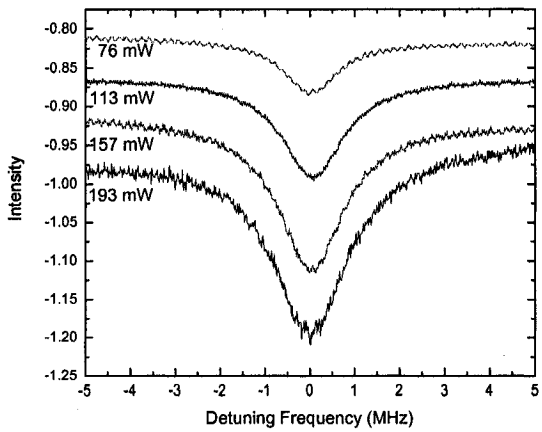

Figure 36: Saturated Absorption Line Profiles of P(16) $^{13}C_2H_2$ at Various Intracavity Power Values. This figure shows several profiles of the saturated absorption line that were captured at various values of intracavity power between 75-200 mW and cavity pressure of 20 mTorr.

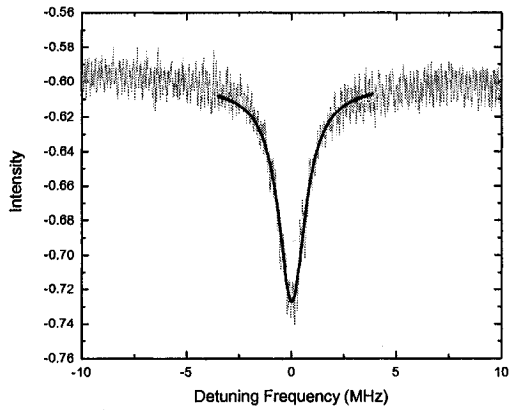

Figure 37: Saturated Dip of P(16) $^{13}C_2H_2$ with Lorentz Fit. This profile was obtained by recording the transmitted light through a Fabry-Perot cavity filled with 20 mTorr of $^{13}C_2H_2$ and intracavity power of 113.40 ± 11.3 mW. The profile was fit within the range of the saturated dip with a Lorentz function. The value of the line width for this profile is 1.45 ± 0.03 MHz.

The square of the line width of the saturation dip, $(FWHM)^2$, is plotted against intracavity power, with its linear regression. This plot is presented in **Figure 38** for the P(16) transition of $^{13}C_2H_2$.

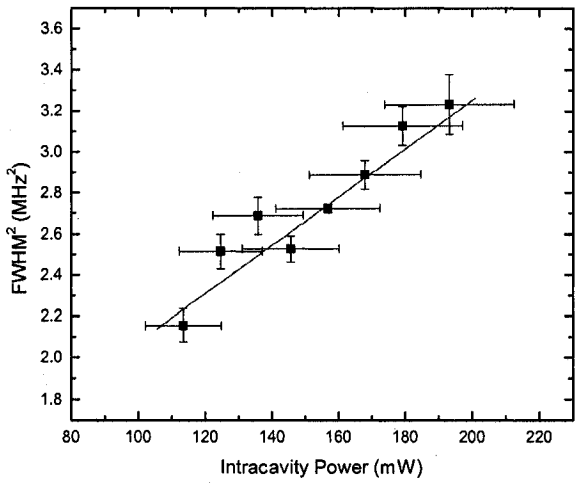

Figure 38: $(FWHM)^2$ vs. Intracavity Power for the Saturated Absorption of P(16) $^{13}C_2H_2$. This figure illustrates the linear regression analysis of the plot of $(FWHM)^2$ vs. Intracavity Power. The slope value for the linear regression is 0.012 ± 0.001 MHz^2/mW and the intercept is 0.9 ± 0.2 MHz^2.

From the slope and intercept of this plot, the values of line width, γ, and saturation power, P_0, are calculated to be $\gamma = 0.95 \pm 0.36$ MHz and $P_0 = 75 \pm 17$ mW, respectively. Profiles of the saturated absorption line at selected values of intracavity powers for the P(16) transition of $^{12}C_2H_2$ are presented in **Figure 39**.

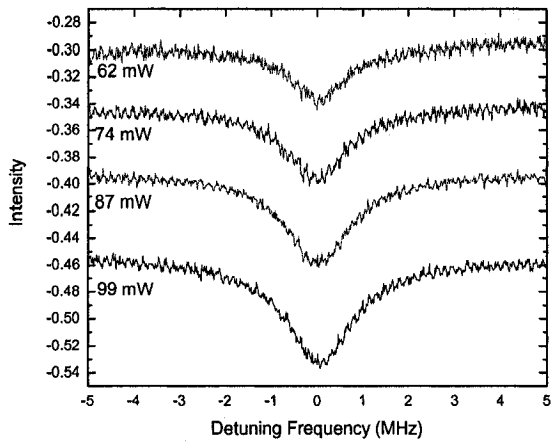

Figure 39: Saturated Absorption Line Profiles of P(16) $^{12}C_2H_2$ at Various Intracavity Power Values. This figure shows several profiles of the saturated absorption line that were captured at various values of intracavity power between 60-100 mW and cavity pressure of 20 mTorr.

A plot of the square of the measured line width, $(FWHM)^2$, versus intracavity power is presented in **Figure 40**.

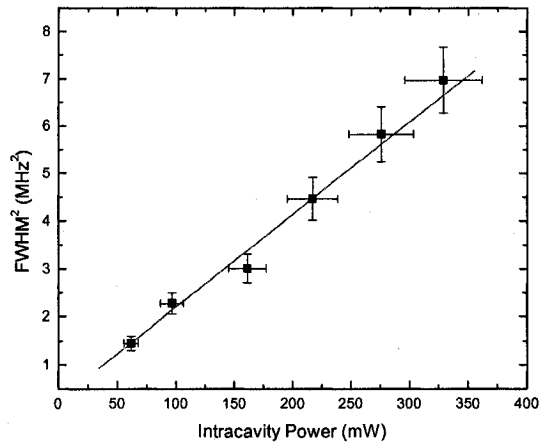

Figure 40: $(FWHM)^2$ vs. Intracavity Power for the Saturate Absorption of P(16) $^{12}C_2H_2$. This figure illustrates the linear regression analysis of the plot of $(FWHM)^2$ vs. Intracavity Power. The slope value for the linear regression is 0.019 ± 0.002 MHz^2/mW and the intercept is 0.26 ± 0.2 MHz^2.

From the slope and intercept of this plot (**Figure 40**), the values of natural line width and saturation power are calculated to be $\gamma = 0.5 \pm 0.3$ MHz and $P_0 = 14 \pm 11$ mW.

Profiles of the saturated absorption line at selected values of intracavity powers for the absorption line at 1531.65 nm of NH_3 are presented in **Figure 41**.

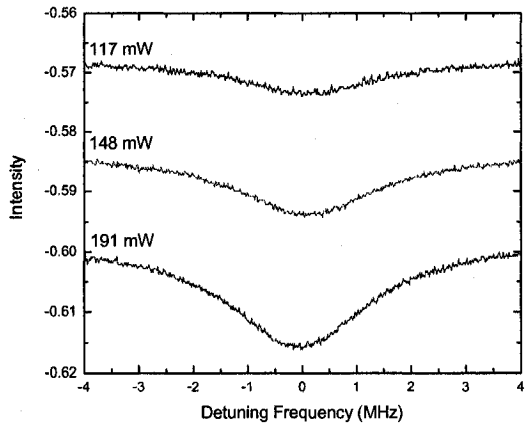

Figure 41: Saturated Absorption Line Profiles for the Transition at 1531.65 nm of NH_3 at Various Intracavity Power Values. This figure shows several profiles of the saturated absorption line that were captured at various values of intracavity power between 230-900 mW and cavity pressure of 20 mTorr.

A plot of the square of the Half-width-at-half-max $(HWHM)^2$ against intracavity power, with linear fit, is shown below in **Figure 42** for the saturated absorption line of NH_3 at 1531.65 nm.

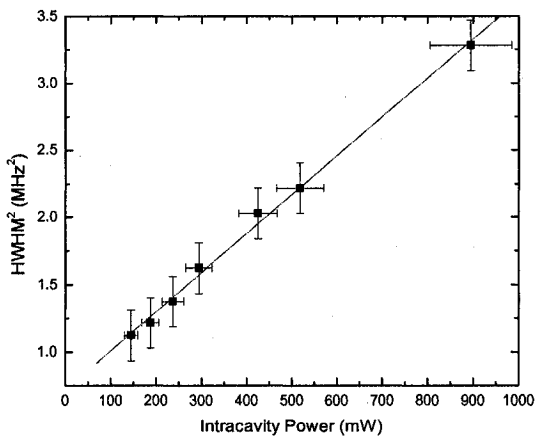

Figure 42: $(HWHM)^2$ vs. Intracavity Power for the Saturate Absorption Line of NH_3 at 1531.65 nm. This figure illustrates the linear regression analysis of the plot of $(HWHM)^2$ vs. Intracavity Power. The slope value is 0.0031 ± 0.0002 MHz^2/mW and the intercept is 0.69 ± 0.05 MHz^2.

The linear regression through this plot yield values of line width, γ, and saturation power, P_0, of: $\gamma = 1.6 \pm 0.3$ MHz and $P_0 = 223 \pm 22$ mW.

To gain insight into the processes responsible for the line broadening in our experiment, one may compare measured linewidth values to the predicted linewidths due to transit time broadening, since this mechanism is the main contributor to line broadening in our experiments using low pressure and slow absorbers. The values of the broadened linewidths due to transit time, $\delta\omega_T$, were calculated using **Eqn. 43**.

These values are presented in **Table 7** for acetylene and ammonia molecules, along with the estimated linewidth from the saturation power broadening experiment.

Table 7: Calculated Linewidths due to Transit Time Broadening and Measured Linewidths.

Molecule: **Line:**	**$^{13}C_2H_2$** **P(16)**	**$^{12}C_2H_2$** **P(16)**	**NH_3** **1531.65 nm**
Calculated $\delta\omega_T$ (kHz)	700	720	910
Measured γ (kHz)	950 ± 360	500 ± 300	1600 ± 300

As may be seen, transit time is responsible for the majority of the linewidth. Taking into account the pressure broadening contribution to be roughly 100-200 kHz, the measured linewidths are easily accounted for in these experiments.

4.7 Estimating the Dipole Moment from Power Broadening Measurements

The dipole moment, μ_{12}, of an absorption line is traditional measured by obtaining a Doppler broadened profile of the line and using the following relation between the spectral intensity, $A(\omega)$, and the magnitude of the dipole moment:

(Eqn. 53) $$\int_{line} A(\omega)d\omega = \frac{8\pi^3\omega_0 N_0(e^{-\frac{E_1}{kT}} - e^{-\frac{E_2}{kT}})(J+1)|\mu_{12}|^2}{3hcQ}$$ [41];

where ω_0 is the central frequency of the line, N_0 is Loschmidt's number, Q is the state sum, E_1 is the energy of the lower state, and E_2 is the energy of the upper state. Typically the dipole moment, μ_{12}, obtained from linear absorption (**Eqn. 53**) allows one to estimate the power necessary to saturate a given transition using **Eqn. 51**. However, if the condition for saturation is already obtained, and one has at their disposal measurements of line broadening at various saturation powers, the dipole moment may also be determined from:

(Eqn. 54) $$|\mu_{12}| = \sqrt{w_0^2\left(\frac{\pi}{4}c\varepsilon_0\frac{(\hbar\gamma)^2}{P_0}\right)}$$ [42].

Using the values of γ and P_0 that were determined experimentally, the dipole moments can be calculated, even without rotational line assignment, from **Eqn. 54**. This method was tested for the P(16) transition of $^{13}C_2H_2$ and the P(16) transition of $^{12}C_2H_2$, for which the values of μ_{12} were known, and then applied to the 1531.65 nm transition in NH_3, for which the precise rotation assignment is unknown. The results are displayed in **Table 8**.

Table 8: Calculated Dipole Moments for Transitions of $^{13}C_2H_2$, $^{12}C_2H_2$, and NH_3.

Molecule	Transition	Dipole Moment, μ_{12} (mD)	Uncertainty (mD)
$^{12}C_2H_2$	P(16)	2.9	0.5
$^{13}C_2H_2$	P(16)	2.4	0.8
NH_3	1531.65 nm	1.6	0.4

The dipole moment that was determined for the P(12) line of the $\nu_1+\nu_3$ band for $^{13}C_2H_2$ by Long-Sheng Ma, Jun Ye, Pierre Dubé, and John L. Hall [42] was 3.018 mD. This value agrees with our results for the dipole moment of the P(16) line of the $\nu_1+\nu_3$ band for $^{13}C_2H_2$ (2.4 ± 0.5 mD) and the P(16) line of the $\nu_1+\nu_3$ band for $^{12}C_2H_2$ (2.9 ± 0.5 mD).

5. Conclusion

Two frequency stabilized laser systems operating in 1510-1580 nm were used to study the parameter shifts for various transitions in $^{12}C_2H_2$ and $^{13}C_2H_2$. These results are summarized in **Tables 9** and **10** [43]. The system's 100 s relative stability was determined to be on the 6×10^{-13} level which is smaller than the reproducibility which was established in earlier experiments to be 8×10^{-12} [11]. Naturally, observed shifts were below the reproducibility limit and as such had to be measured "on the fly" without re-locking of the servos. This effect, combined with the great variation in the signal

strength, is believed to be greatest source of the uncertainty in measured values. It was concluded that in order to measure parameter shifts for ammonia, as well as for other weaker lines of acetylene, further improvements of the electronics servo system are needed.

Table. 9: Parameter Shifts of $^{13}C_2H_2$.

$^{13}C_2H_2$ Line	Power Shift (Hz/mW)	Uncertainty (Hz/mW)	Pressure Shift (Hz/mTorr)	Uncertainty (Hz/mTorr)
P(10)	-11.9	0.8	Not Measured	Not Measured
P(11)	-21.5	1.1	-176	6
P(14)	-19.1	1.6	-433	14
P(15)	-19.8	1.4	-82	8
P(16)	-12.8	0.5	Not Measured	Not Measured
P(20)	-8.8	0.7	-79	10

Table. 10: Parameter Shifts of $^{12}C_2H_2$.

$^{12}C_2H_2$ Line	Power Shift (Hz/mW)	Uncertainty (Hz/mW)	Amplitude Modulation Shift (Hz/MHz)	Uncertainty (Hz/MHz)
P(3)	-16.0	0.9	-437	24
P(4)	-13.8	1.0	-360	76
P(13)	-200	15.0	-1063	61
P(14)	-29.6	2.3	-1284	50
R(8)	-110	7.0	Not Measured	Not Measured

In addition to these results, the power broadening studies for three lines in isotopic acetylene and ammonia were performed. These studies yielded values of saturation parameters and transition dipole moment that were independent from the measurements derived from linear absorption coefficients. These results are summarized in **Table 11**. It needs to be pointed out that the studies of the saturated absorption effect in the near infrared lines of ammonia were performed for the first time, as the effect was just recently discovered [44].

Table 11: Estimated Values of Linewidth, Saturation Parameter, and Dipole Moment.

	Linewidth, γ, (kHz)	**Uncertainty (kHz)**	**Saturation Power, P_0, (mW)**	**Uncertainty (mW)**	**Dipole Moment, μ, (mD)**	**Uncertainty (mD)**
$^{13}C_2H_2$ P(16)	950	360	75	17	2.9	0.5
$^{12}C_2H_2$ P(16)	500	300	14	11	2.4	0.8
NH_3 Transition at 1531.65 nm	1600	300	223	22	1.6	0.4

Appendix

A. Quantitative Description of the Pound-Drever-Hall Lock

To describe the Pound-Drever Lock quantitatively, one may investigate the electric field of the incoming radiation at a point after the electro-optic modulator (EOM). This electric field can be described as:

(Eqn. A1) $E_{inc} = E_0 e^{i(\omega t + \beta \sin \Omega t)}$ [32];

where β is the amplitude of modulation, and Ω is the frequency of modulation.
This expression can be expanded using Bessel functions to illustrate that it is composed of three beams at different frequencies:

(Eqn. A2)

$$E_{inc} \approx \left[J_0(\beta) + 2iJ_1(\beta)\sin\Omega t\right]e^{i\omega t} = E_0\left[J_0(\beta)e^{i\omega t} + J_1(\beta)e^{i(\omega+\Omega)t} - J_1(\beta)e^{i(\omega-\Omega)t}\right]$$

[32].

After reflection from the F-P cavity, E_{ref}, is composed of these three beams each multiplied by the frequency dependent reflection coefficient, F(ω):

(Eqn. A3)

$$E_{ref} = E_0\left[F(\omega)J_0(\beta)e^{i\omega t} + F(\omega+\Omega)J_1(\beta)e^{i(\omega+\Omega)t} - F(\omega-\Omega)J_1(\beta)e^{i(\omega-\Omega)t}\right]$$

[32].

The reflection coefficient is the ratio of E_{ref}/E_{inc} and for a symmetric cavity with no losses it is:

(Eqn. A4) $$F(\omega) = \frac{r\left(\exp\left(i\frac{\omega}{FSR}\right)-1\right)}{1-r^2\exp\left(i\frac{\omega}{FSR}\right)}$$ [32];

where r is the amplitude reflection coefficient of each mirror, and FSR is the free spectral range of the cavity.

What the photo detector measures is the power of the radiation:

(Eqn. A5) $$P_{ref} = \left|E_{ref}\right|^2$$ [32].

Since E_{ref} is composed of three beams the detector measures:

(Eqn. A6)

$$P_{ref} = P_c\left|F(\omega)\right|^2 + P_s\left\{\left|F(\omega+\Omega)\right|^2 + \left|F(\omega-\Omega)\right|^2\right\} +$$
$$2\sqrt{P_sP_c}\left\{\mathrm{Re}\left[F(\omega)F^*(\omega+\Omega) - F(\omega)F^*(\omega-\Omega)\right]\cos\Omega t + \mathrm{Im}\left[F(\omega)F^*(\omega+\Omega) - F(\omega)F^*(\omega-\Omega)\right]\sin\Omega t\right\}$$
$$+ (2\Omega terms)$$

where $P_c = J_0^2(\beta)P_0$, $P_s = J_1^2(\beta)P_0$, and $P_0 \equiv \left|E_0\right|^2$ [32].

The result of combining these three waves at frequencies of ω, and ω ± Ω is that the photo detector will resolve a beat pattern from interference of the carrier wave frequency with each sideband, as well as the beat between the two sidebands. The components that require our attention are the beat frequencies at Ω and not the 2 Ω terms. The Ω terms are of interest because they contain information about the phase of the reflected carrier wave. These Ω terms are:

(Eqn. A7) $\sin(\Omega t)$ and $\cos(\Omega t)$ [32].

Depending on the modulation frequency, usually one of these terms vanishes and one remains.

The signal from the photo detector is then "mixed down" with a mixer using a local oscillator at frequency Ω'. If the input to the mixer is sin(Ωt), the output is:

(Eqn. A8) $\sin(\Omega t)\sin(\Omega' t) = \frac{1}{2}\{\cos[(\Omega-\Omega')t]-\cos[(\Omega-\Omega')t]\}$ [32].

If the local oscillator is regulated to the frequency of modulation (Ω'= Ω), then the cos((Ω-Ω')t) term becomes a dc signal. In the case that the input signal to the mixer is cos(Ωt), it is useful, in practice, to phase shift the signal by 90° to become sin(Ωt) to obtain the dc signal. This term is then isolated by conveying the signal through a low-pass filter.

In the condition that the carrier frequency is very close to resonance of the Fabry-Perot cavity, and modulation is adjusted so that the sidebands are not at the point of cavity resonance, the sidebands are completely reflected from the cavity and the carrier frequency has no reflection. In this special case, we may simplify **Eqn. A6** using:

(Eqn. A9) $|F(\omega)|^2 \approx 0$ and $F(\omega \pm \Omega) \approx -1$ [32].

These simplifications yield the approximation of the error signal as:

(Eqn. A10) $P_{ref} \approx 2P_s - 4\sqrt{P_c P_s}\,\mathrm{Im}\{F(\omega)\}\sin(\Omega t) + (2\Omega terms)$ [32];

where P_c and P_s are defined above.

A plot of the error signal is presented in **Figure A1**:

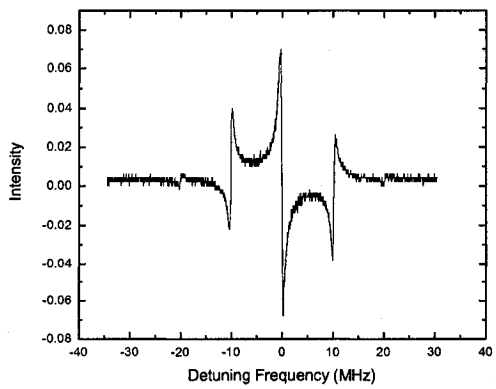

Figure A1: Pound-Drever-Hall Error Signal. The signal has zero intensity when the laser frequency is equal to cavity resonsance.

B. A Quantitative Description of Obtaining the Harmonics from the Lock-In Amplifier

To understand how the lock-in amplifier generates the 3f signal from the saturated dip of an absorption line, consider initially describing the saturate dip profile mathematically by a parabolic function for the central region of a Doppler broadening line and a Taylor expansion Gaussian function about ω_0 for the absorption dip:

(Eqn. B1) $$I(\omega) = A\omega^2 + B\omega + C + \frac{D}{(\omega - \omega_0)^2 + (\gamma/2)^2}$$ [29];

where A, B, C, and D are constants and γ is the linewidth of the saturation dip.
The lock-in amplifier then applies a small amount of modulation to the cavity at modulation frequency Ω. This modulation is small enough that it is on the order of the bandwidth of the saturated absorption dip. We may further develop our mathematical description of the Doppler-broadened profile by using a Taylor expansion about the carrier frequency plus modulation (i.e. $\omega_0 + a\sin\Omega t$, where "a" is the modulation amplitude). Through a bit of algebra and trigonometric relations, one obtains the relation:

(Eqn. B2)
$$\begin{aligned} I(\omega) \cong\ & I(\omega_0) + \frac{a^2}{4} I^{(2)}(\omega_0) + \frac{a^4}{64} I^{(4)}(\omega_0) + \ldots \\ & + \left[a I^{(1)}(\omega_0) + \frac{a^3}{8} I^{(3)}(\omega_0) + \ldots \right] \sin\Omega t \\ & + \left[-\frac{a^2}{4} I^{(2)}(\omega_0) - \frac{a^4}{48} I^{(4)}(\omega_0) + \ldots \right] \sin 2\Omega t \\ & + \left[-\frac{a^3}{24} I^{(3)}(\omega_0) - \frac{a^5}{384} I^{(5)}(\omega_0) + \ldots \right] \sin 3\Omega t \\ & + \ldots \end{aligned}$$

where $I^{(n)}(\omega) = \dfrac{d^n I(\omega)}{d\omega^n}$ [29].

This form illustrates the profile in expressions of harmonics, where the n^{th} harmonic is the term in front of sin(nΩt). Also, since the modulation amplitude is typically small in experiments, the dominant term in the n^{th} harmonic is the first term in the brackets in front of the sin(nΩt) term (in **Eqn. B2**). Thus the n^{th} harmonic is, in good approximation, a constant times the n^{th} derivative of I(ω).

The third harmonic, in particular, is an important harmonic. To establish this importance, let's consider the profiles of the first three harmonics, or derivatives, of the original function $I(\omega)$: $I^{(1)}(\omega)$, $I^{(2)}(\omega)$, and $I^{(3)}(\omega)$.

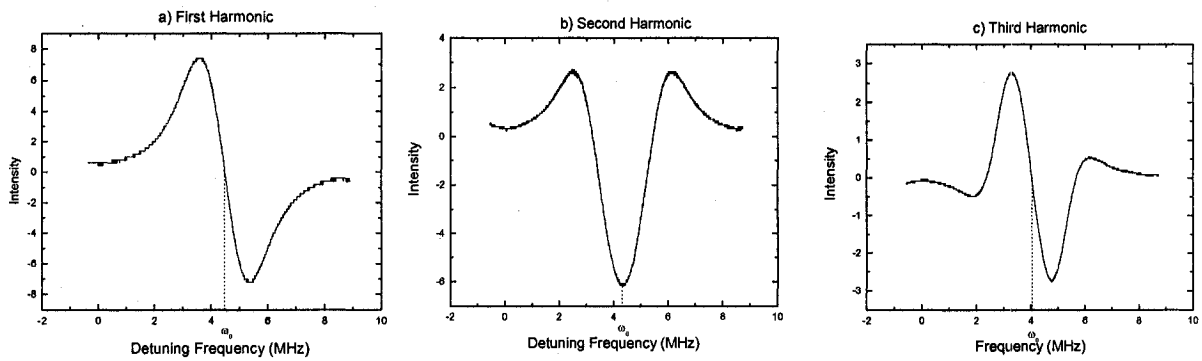

Figure B1: Profiles of the Harmonics. In figures a, b, and c profiles of the first, second and third harmonics are shown. By demodulating the signal from the photo detector at 1-f, 2-f, and 3-f one obtains the first, second and third harmonic respectively.

Some of these harmonics (**Figure B1**) provide a suitable characteristic to lock and stabilize the laser frequency onto the absorption line at ω_0. Compared with the first three harmonics, the third harmonic is the best of these for several reasons: the original function may contain an offset in background from the Doppler broad line and this offset, although reduced from a derivative, may still exist within the $I^{(1)}(\omega)$ signal. The second harmonic is symmetric about ω_0. This characteristic designates the $I^{(2)}(\omega)$ signal as an unsuitable candidate for the error signal because it cannot inform the servo which

direction to steer the laser frequency to maintain on top of the saturation dip. However, the third harmonic is symmetric about the central point of the saturation dip, ω_0, it eliminates more of an existing offset of the original function than the first harmonic, and it has the strongest dependency on frequency (compared to the first and second harmonics) about ω_0. For these reasons, this signal provides more accurate steering and less overshoot during stabilizing. The fifth harmonic is also a suitable candidate for the error signal, however this harmonic is generally more difficult to use in practice because the signal to noise ratio becomes reduced with increasing harmonics.

C. Measuring Doppler-Broadened Absorption Spectra of C_2H_2 and NH_3

Profiles of the Doppler-broadened absorption spectra of C_2H_2 and NH_3 were acquired using a linear absorption cell apparatus with long and short wavelength scan techniques as described earlier.

Figure C1 shows the measured intensity of transmitted light between 1510 – 1520 nm through a 1 m long absorption cell filled with 10 Torr of NH_3. The profile was obtained using the scan option on the commercial laser (New Focus) in System 1.

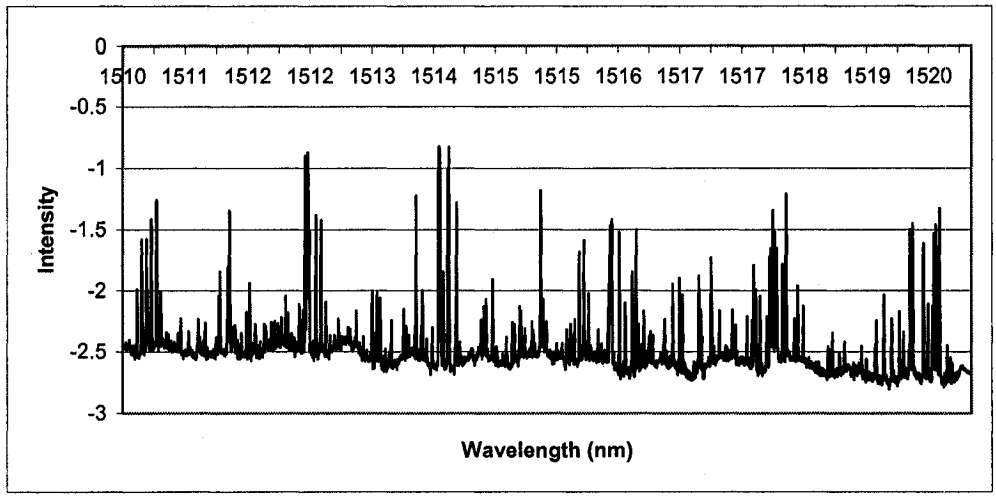

Figure C1: Transmitted Light from Absorption Cell. This figure illustrates the un-normalized plot of transmitted intensity versus wavelength. Measurements were taken by recording the signal intensity from the photo detector while scanning the laser wavelength over the given range. Laser output power was set to 13.1 mW and cell pressure was 10 Torr of NH_3.

As can be seen from plot in **Figure C1**, the background intensity is not constant but varying over wavelength. The fluctuating background is also apparent throughout scanning over the 1510 – 1560 nm spectrum. This result is most likely due to the output power of the laser fluctuating while scanning through wavelength. It is possible that this variation of output power is due to wavelength dependent reflection of some of the coating and mirrors within the internal composition of the laser.

Regardless of the cause of the intensity fluctuation, relative intensities should be plotted with constant background. For this reason, the Doppler-broadened absorption apparatus includes a well-placed beam splitter and two photo detectors. One photo detector measures the intensity of the laser beam without any absorption while the secondary photo detector simultaneously measures the intensity of the beam after absorption. A plot of the laser performance without absorption for the 1510 – 1520 nm region is shown in **Figure C2**.

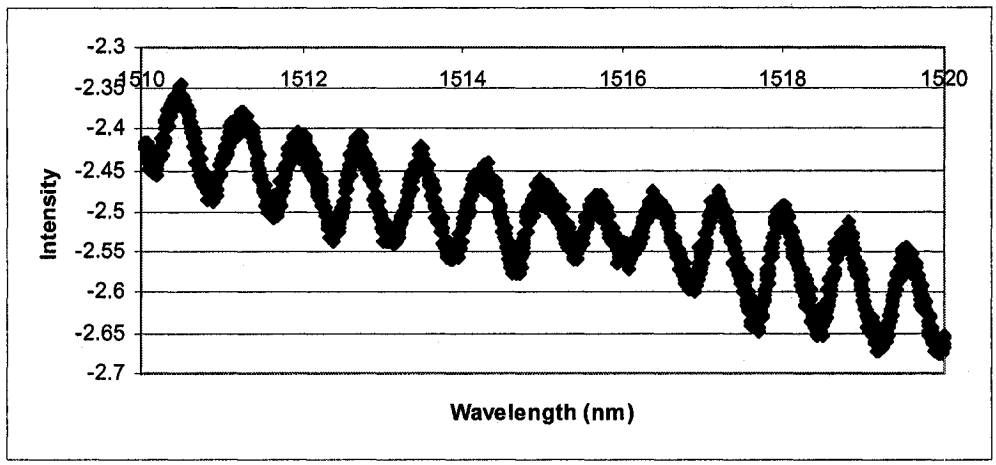

Figure C2: Laser Beam Intensity Without Absorption. Power fluctuations of the laser performance over wavelength were observed and monitored with a photo detector. System settings were 13.1 mW on laser output and 10 Torr of NH_3 cell pressure.

The plot in **Figure C2** shows that the output power of the laser is oscillating regularly and decreasing with increasing wavelength. The fact that these oscillations are regular leads one to believe that this is due to an interference effect within the cavity of the commercial laser.

Even without determining the exact origin of the laser output behaviour, and avoiding disassembling the laser, the data collected from the photo detectors was used to construct an absorption spectrum of the gas with near constant background. The profile of the laser output without absorption (**Figure C2**) was manipulated by scaling the amplitude and adjusting the horizontal shift. These parameters were adjusted to fit, as best as possible (by eye), the background of the profile of the beam intensity with absorption (**Figure C1**). After this data was fit, the background oscillation was then subtracted from the absorption profile to generate the new absorption profile with near constant background.

The relative improvement to the profile of the 1510-1520 nm section (**Figure C1**) is presented in **Figure C3**.

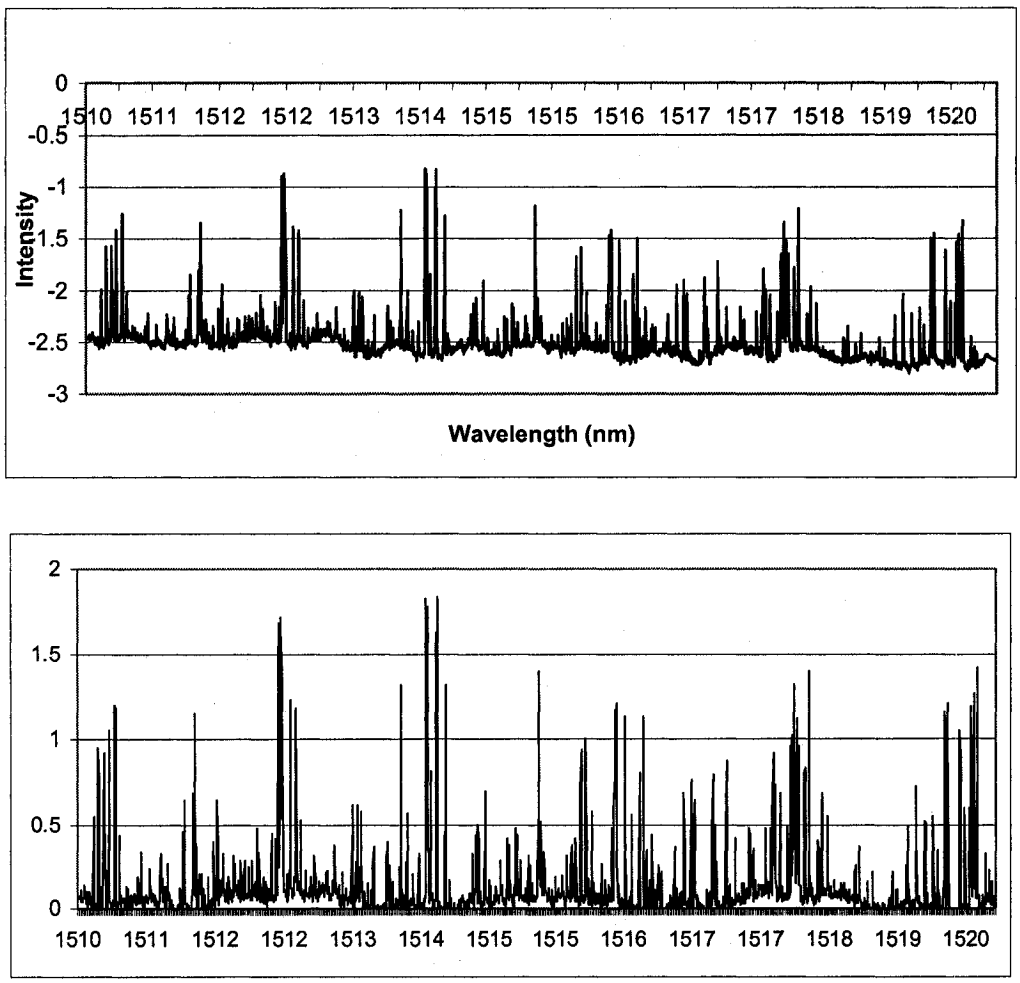

Figure C3: Background Noise Comparison of Adjusted Profile. The two plots (top and bottom) illustrate the improvement accomplished by subtracting the oscillating noise. The top profile is before adjustment. The bottom profile is the same profile after subtracting the oscillating noise, which is also adjusted to have the background at zero intensity.

References

[1] J L. Hall, SPIE 1837 (1992).

[2] D. Adam, Nature. 421 (2003) 207.

[3] P. Gill, G.P. Barwood, H.A. Klein, G. Huang, S.A. Webster, P.J. Blythe, K. Hosaka, S.N. Lea, H.S. Margolis, Meas. Sci. Technol. 14 (2003) 1174.

[4] D.J. Berkeland, J.D. Miller, J.C. Bergquist, W.M. Itano, D.J. Wineland, Phys. Rev. L. 80 (1998) 2089.

[5] G. Santarelli, Ph. Laurent, P. Lemonde, A. Claion, Phys. Rev. L. 82 (1999) 4619.

[6] S. Bize, Y. Sortais, M.S. Santos, C. Mandache, A. Clairon, C. Salomon, Europhys. Lett. 45 (1999) 558.

[7] T. Ido, H. Katori, Phys. Rev. L. 91 (2003) 053001.

[8] J. L. Hall, L-S. Ma, M. Taubman, B. Tiemann, F-L. Hong, O. Pfister, J. Ye, IEEE 48 (1999) 583.

[9] P. Alcantara Jr, L. Guidoni, A. Barsella, A. Fioretti, E. Arimondo, J. Opt. Soc. Am. B 12 (1995) 1326.

[10] S. L. Gilbert, W. C. Swann, T. Dennis, SPIE 4269 (2001) 184.

[11] A. Czajkowski, A.A. Madej, P. Dubé, Opt. Commun. 234 (2004) 259.

[12] M. de Labachelerie, K. Nakagawa, Y. Awaji, M. Ohtsu, Opt. Lett. 20 (1995) 572.

[13] K. Nakagawa, M. de Labachelerie, Y. Awaji, M. Kourogi, J. Opt. Soc. Am. B 13 (1996) 2708.

[14] T.J. Quinn, Metrologia 40 (2003) 103.

[15] A. Onae, T. Ikegami, K. Sugiyama, F.-L. Hong, K. Minoshima, H. Matsumoto, K. Nakagawa, M. Yoshida, S. Harada, Opt. Commun. 183 (2000) 181.

[16] A. Czajkowski, J.E. Bernard, A.A. Madej, R.S. Windeler, Appl. Phys. B. 79 (2004) 45

[17] J.I. Steinfeld, "Molecules and Radiation: An Introduction to Modern Molecular Spectroscopy," Dover Reprint Edition, MIT Press (2005).

[18] Jack. D. Greybeal, "Molecular Spectroscopy," Revised First Edition, McGraw-Hill, New York (1988)

[19] C.W. Garland, J.V. Nibler, D.P. Shoemaker, "Experiments in Physical Chemistry," Seventh Edition, McGraw-Hill, New York (2003).

[20] Massachusetts Institute of Technology, Department of Chemistry, 5.33 Advanced Chemical Experimentation and Instrumentations, "Experiment #1: Molecular Spectroscopy of Acetylene and Methane," (2005).

[21] M. E. Webber, D.S. Baer, R.K. Hanson, Appl. Opt. 40 (2001) 2031.

[22] E.D. Williams, R.U. Ayres, M. Heller, Environ, Sci, Technol. 36 (2002) 5504.

[23] D.G. Lancaster, D. Richter, R.F. Curl, F.K. Tittel, Appl. Phys. B 67 (1998) 339.

[24] J.B. Dalton, J.M. Curchin, R.N. Clark, Lunar and Planetary Science XXXII (2001) 1496.

[25] F.K. Tittel, D. Weidmann, C. Oppenheimer, L. Gianfrani, Optics and Photonics News 17 (2006) 24.

[26] Z. Bozóki, A. Mochácsi, G. Szabó, Z. Bor, M. Erdélyi, W. Chen, F.K. Tittel, Appl. Spec. 56 (2002) 715.

[27] G. Berden, R. Peters, G. Meijer, Chem. Phys. Lett. 307 (1999) 131.

[28] L. Lundsberg-Nilesen, F. Heglund, F.M. Nicolaisen, Journ. Mol. Spec. 162 (1993) 230.

[29] W. Demtroder, "Laser Spectroscopy: Basic Concepts and Instrumentation," Springer-Verlag, Berlin, (1982).

[30] K. Shimoda, "Topics in Applied Physics: High-Resolution Laser Spectroscopy," Springer-Verlag, Berlin, (1976).

[31] V. A. Alekseev, T. L. Andreeva, I. I. Sobel'man, Sov. Phys.-JETPn 37 (1973) 413.

[32] E. Black, Am. J. Phys. 69 (2001) 79.

[33] K. Shimoda, A. Javan, J. Appl. Phys. 36 (1965) 718.

[34] R. Balhorn, H. Kunzmann, F. Lebowsky, Appl. Optics. 11 (1972) 742.

[35] J. Jiang, A. Onae, H. Matsumoto, F.-L. Hong, Opt. Soc. Am. 13 (2005) 1958.

[36] C.S. Edwards, H. S. Margolis, G.P. Barwood, S.N. Lea, P. Gill, G. Huang, W.R.C. Rowley, Opt. Lett. 29 (2004) 566.

[37] M. Kusaba, J. Henningsen, J. Mol. Spectrosc. 209 (2001) 216.

[38] P. Balling, Opt. Soc. Am. 13 (2005) 9196.

[39] M. Gläser, Metrologia. 23 (1986) 45.

[40] S.L. Gilbert, W.C. Swann, C.M. Wang, "Hydrogen cyanide $H^{13}C^{14}N$ absorption reference for 1530-1560 nm wavelength calibration" – SRM 2519, NIST Spec. Publ. 260-137, National Institute of Standards and Technology, Gaithersburg, MD, (1998).

[41] M. Trefler, H.P. Gush, Phys. Rev. L. 20 (1968) 703.

[42] L.-S. Ma, J. Ye, P. Dubé, J.L. Hall, J.Opt. Soc. Am. B. 16 (1999) 2255.

[43] Czajkowski, M.Corrigan, J.Bernard, A. Madej. "Paremeter shifts measurements for several metrology-relevant lines in $^{12}C_2H_2$ and $^{13}C_2H_2$," submitted to Optics Letters (2006).

[44] Czajkowski, J.Alcock, J.Bernard, A.Madej. "First observation of Saturated Absorption in near infrared ammonia transitions and their frequency measurements using Cr^{4+}:YAG frequency comb," submitted to Optic Letters (2006).